

Abstract

The socioeconomic losses from the recent unpreceded incidents in the electric power systems suggest the need for alternative planning strategies that account for the expected and extreme events that are less likely to occur. Such high impact low probability (HILP), or black swan, events are typically weather-related, have accounted for billions of dollars in economic losses, and left customers in the dark for several days. Furthermore, the proliferation of distributed energy resources (DERs) on the distribution grid indicates that system operators can also plan resilience from the customer's end, forming intentional microgrid islands when needed. However, existing planning strategies only minimize the expected operating cost and do not explicitly include the risk of extreme events. With the increasing frequency of black swan events in the current scenario, system operators should focus on the HILP events and find the optimal trade-off decision to maximize resilience with available resources. This proposal aims to investigate the impact of extreme weather events, hurricanes, and floods, on the power grid and propose planning solutions to enhance the grid's resilience. Firstly, we propose a modeling framework to assess the spatiotemporal compounding effect of hurricanes and storm surges on electric power systems. The spatiotemporal probabilistic loss metric helps system operators identify the potential impact and vulnerable components as the storm approaches. Secondly, we develop a risk-averse two-stage stochastic optimization framework for resilience planning of power distribution systems against extreme weather events. The resource planning strategy involves minimizing a risk metric, conditional value-at-risk (CVaR) while adhering to budget constraints for planning. The main idea is to identify a trade-off between risk-averse and risk-neutral planning solutions to maximize the energization of critical loads when a HILP event is realized. The problem is also extended to determine the trade-off among different resources when system operators have a limited budget. This facilitates the selection of specific resources from a portfolio of various resources that can optimally restore critical loads during the realization of a HILP event. In the future, the work will be extended to a larger and broader landscape with an analysis based on realistic extreme weather events and their impact on the power system. The goal will be to create a generic simulation platform capable of generating and assessing the impact of such events on the electric power grid. The work will also include large-scale integrated operational solutions to enhance the resilience of future power grids. Furthermore, advanced parallel algorithms based on dual decomposition methods will be explored for scalable implementation of stochastic programming problems.

Contents

1 Motivation	4
2 Objectives and Task Lists	6
2.1 Risk-based Resilience Quantification using Multi-criteria Decision Making	7
2.1.1 Prior work in Resilience Metric and Their Limitations	7
2.1.2 Proposed Risk-based Resilience Metric	8
2.1.3 Resilience-driven Parameters and Metrics: Definition	8
2.1.4 Probabilistic Event and Impact Assessment	12
2.1.5 Preliminary Research Results	14
2.2 Risk-based Resilience Planning of Power Distribution Systems	17
2.2.1 Prior work on Power Distribution Planning and their limitations	17
2.2.2 Planning Problem Representation	19
2.2.3 Problem formulation	20
2.2.4 Proposed scenario generation and selection approach	22
2.2.5 Preliminary Research Results	24
3 Spatiotemporal impact assessment of hurricanes and storm surges in electric power systems	35
3.1 Prior work on extreme weather impact assessment on power systems and their limitations	35
3.2 Proposed Approach and Modeling	35
3.2.1 Hurricane Wind field Model	35
3.2.2 Storm Surge Model	37
3.2.3 Impact Model	38
3.3 Event Generation and Impact Assessment Framework	39
3.3.1 Hurricane and Storm Surge Scenario Generation	41
3.3.2 Power Systems Impact Assessment	42
3.4 Preliminary Research Results	43
4 Temporal Alternating Direction Method of Multipliers (tADMM)	46
4.1 Introduction and Motivation	46
4.2 LinDistFlow MPOPF with tADMM	47
4.2.1 Problem Overview	47
4.2.2 Variable Color Coding	47
4.2.3 Sets and Indices	47
4.2.4 tADMM Algorithm Structure	48
4.2.5 Convergence Criteria	50
4.3 Copper Plate MPOPF with tADMM (Simplified Case)	51

4.3.1	Problem Overview	51
4.3.2	Variable Color Coding	51
4.3.3	tADMM Algorithm Structure	51
4.4	Numerical Results	54
4.4.1	Battery Actions and Convergence Analysis	54
4.5	Convergence Criteria	55
4.5.1	Convergence Criteria	55
4.6	Algorithm Parameters	56
4.6.1	Objective Function Components	56
4.6.2	Algorithmic Parameters	57
4.7	Appendix: Full Variable and Parameter Definitions	57
4.7.1	System Bases	57
4.7.2	SOC Bound Definitions	57
4.7.3	Physical Interpretation	57
4.8	Summary and Discussion	58
4.8.1	Implementation Status	58
5	Future Works	61
5.1	Task 1: Temporal Decomposition for Medium Sized Balanced Three-Phase Systems	61
5.2	Task 2: Temporal Decomposition for Large Sized Unbalanced Three-Phase Systems	61
5.3	Task 3: Concluding Research and Dissertation	62
5.4	Timeline	63
6	Biography	64
6.1	Publications	64
6.2	Program of Study Course Work	65
Appendix		66
.1	Full MPOPF Formulation with LinDistFlow	66

1 Motivation

Optimal power flow (OPF) methods have become vital for efficiently managing distributed energy resources (DERs) such as photovoltaic (PV) and battery energy storage systems (BESS) at the grid edge, aiming to enhance system-level objectives including reliability, resilience, and cost-effectiveness [1, 2]. BESS, by mitigating the fluctuations of intermittent DERs, transforms the OPF problem from a classic single-period formulation into a multi-period, time-coupled optimization that demands intricate modeling and advanced computational methods [1, 3].

Centralized OPF (COPF) approaches typically rely on non-convex formulations—often based on the nonlinear branch flow model [4]—to coordinate controllable devices. Although such methods can provide accurate solutions for small networks [1, 3, 5], computational time and scalability issues limit their utility in large-scale, real-world systems. Metaheuristic and evolutionary algorithms [6] offer alternative solutions but generally struggle with local optimality and slow convergence, especially for high-dimensional multi-period OPF tasks.

To improve tractability, convex relaxations and linear approximations such as LinDistFlow [7] have been widely employed [1, 3, 7]. These methods deliver fast convergence but introduce non-negligible optimality gaps, particularly as network size and DER/BESS penetration increase, which has not been fully quantified in existing research [1]. Recent studies have highlighted this gap, advocating for a systematic comparison of non-convex and linearized frameworks across varied network conditions [1, 7].

Recognizing the limitations of centralized and linear-programming-based solutions, recent research—including our own—has focused on spatial and temporal decomposition for scalable multi-period OPF. Our group adapted the Equivalent Network Approximation (ENApp) framework to enable distributed MPOPF (MPDOPF) in battery-integrated networks, leveraging spatial partitioning to allow parallel solution of local OPF subproblems and reduce global computational burdens [8]. This approach harnesses the radial structure of distribution networks and significantly accelerates convergence while maintaining solution fidelity. Moreover, our models introduce a battery loss term exclusively in the objective function, preventing simultaneous charge/discharge operations and preserving problem convexity without integer variables [8].

Extensive validation against industry-standard IEEE test systems demonstrates that our ENApp-based distributed MPOPF delivers superior scalability and optimality compared with conventional centralized frameworks. These studies also provide a robust, side-by-side comparison of LinDistFlow and branch flow-based nonlinear models for MPOPF across real

distribution network scenarios [1].

Major remaining research gaps include the scalability and real-time applicability of centralized MPOPF approaches [3, 5, 9–11], and the slow convergence and master controller dependencies in existing distributed frameworks such as Benders decomposition [12]. The contribution of this work is the development and benchmarking of a spatially distributed multi-period OPF algorithm, overcoming these challenges and enabling practical, accurate, large-scale coordinated grid-edge resource management.

2 Objectives and Task Lists

The overarching goal of this work is to develop a computationally scalable framework for solving the Multi-Period Optimal Power Flow (MPOPF) problem in active distribution systems. The proposed framework aims to address the inherent complexity and non-convexity of MPOPF formulations – arising from temporal coupling of decision variables and high-dimensional system models – by designing and implementing decomposition-based algorithms. The resulting framework is expected to enable tractable and near-optimal solutions for realistic time horizons and large distribution feeders, while preserving the physical fidelity of the underlying models. The following tasks have been completed or are currently being pursued toward achieving the objectives of this study:

1. **Literature Review on Multi-Period Optimal Power Flow:** A comprehensive review was conducted on existing formulations of the MPOPF problem for active distribution systems. This provided insights into modeling temporal dependencies, handling storage dynamics, and integrating distributed energy resources in multi-period settings.
2. **Study of Decomposition-Based Optimization Techniques:** A review of decomposition algorithms, including Bilevel optimization methods, ADMM, and Differential Dynamic Programming (DDP), was carried out to understand their suitability for large-scale and temporally coupled optimization problems. The study highlighted key convergence properties and trade-offs between spatial and temporal decompositions.
3. **Implementation of Spatial Decomposition for MPOPF:** A spatially decomposed MPOPF formulation was implemented and tested on benchmark distribution systems. The method demonstrated improved scalability compared to monolithic optimization, though it remained limited in addressing the temporal coupling present in long-horizon studies.
4. **Development and Evaluation of Differential Dynamic Programming (DDP):** The DDP algorithm was formulated and implemented for the MPOPF problem. While the approach yielded solutions close to those obtained from brute-force optimization, it exhibited oscillatory convergence behavior and lacked strong theoretical guarantees. Further research is required to enhance its stability and convergence properties.
5. **Implementation of Temporal ADMM for MPOPF:** A temporal Alternating Direction Method of Multipliers (ADMM) approach is being developed to address the

scalability challenges associated with increasing time horizons. Preliminary results on a copper-plate system show excellent convergence, and current efforts focus on extending the implementation to LinDistFlow-based distribution models.

6. **Validation and Scalability Testing:** The final phase will involve validating the proposed algorithms on a large-scale system like the 9500-node (three-phase) feeder. The goal is to demonstrate the framework's scalability for realistic horizons (e.g., $T = 96$ i.e. 1 day at 15-minute intervals) and its applicability to operational optimization in distribution grids.
7. **Exploratory Study on Multiple-Source Optimal Power Flow (MS-OPF):** As a future research direction, the framework will be extended to accommodate multi-source configurations, enabling coordinated optimization across multiple substations and zones in distribution networks.

2.1 Risk-based Resilience Quantification using Multi-criteria Decision Making

2.1.1 Prior work in Resilience Metric and Their Limitations

In literature, multiple articles have sought to define the resilience metrics and have proposed several methods to solve the resilience planning problem. The existing metrics for resilience can be broadly categorized as: a) attribute-based metrics that identify power system attributes such as robustness, resourcefulness, adaptivity, recoverability, and situational awareness [13] and b) performance-based metrics that describes the system's ability to maintain supply (i.e., the system's availability [14]) and often measured using the conceptual resilience curve [15]. Different resilience indicators that are widely used in literature are based on the optimal repair time of critical components [16], energy not served after an extreme event [17], total critical loads supplied during the aftermath of a disaster [18], and in terms of infrastructure recovery [19]. The resilience of power distribution systems is dependent on several factors such as network configuration, available resources and controls, and several other smart grids features such as distributed energy resources (DERs), smart switches, intentional islanding, and self-healing. Towards this goal, references [20, 21] introduce the use of multi-criteria decision-making (MCDM) methods to quantify resilience by taking different topological parameters based on graph theory.

Despite these existing approaches no formal resilience metric is universally accepted. The existing metrics to quantify power distribution system resilience pose one or more limitations including: (1) they are post-event measures and mostly evaluated for a single event [16,18,22]; (2) they do not specifically measure the impacts of HILP events on system performance (kW loss, critical assets without power, total outage duration) [20, 21]; (3) they do not provide additional flexibility to system operators to prioritize one investment decision over the other to evaluate the system resilience [23].

2.1.2 Proposed Risk-based Resilience Metric

In contrary to reliability assessment, events with higher impact and lower probability are considered for resilience analysis [24]. Thus, this dissertation proposes a probabilistic approach to calculate the resilience metric that captures both the system attributes as well as its response to a given extreme event. Prior to this work, our group proposed a framework to evaluate the resilience of power distribution systems using conditional value-at-risk as a risk measure [25]. The specific contributions are listed below:

1. *Multi-criteria Risk-based Resilience Metric:* A novel risk-based resilience metric that considers a comprehensive power system resilience definition. The proposed metric takes multiple resilience-driven parameters – availability, robustness, brittleness, resistance, and resourcefulness to holistically evaluate the power distribution system resilience based on these parameters.
2. *Comprehensive Simulation Framework for Resilience Quantification:* A simulation-based approach that allows system operators to evaluate different mitigating actions. The proposed framework provides additional flexibility to prioritize one investment decision over the others to enhance the system's resilience; The operators can come up with economic investment decisions without compromising the resilience of the system.

2.1.3 Resilience-driven Parameters and Metrics: Definition

2.1.3.1 Resilience Parameters: Fig. 1 shows a typical resilience assessment curve in which the x -axis represents time whereas the y -axis represents the number of weighted CLs online. Let N_C be the total number of CLs that are online at a particular instance of time. The time in which all of the CLs remain online to the time an event occurs is denoted by $T_{1,U}$ and represented by phase 1. In this work, $T_{1,U}$ is considered the same for all CLs.

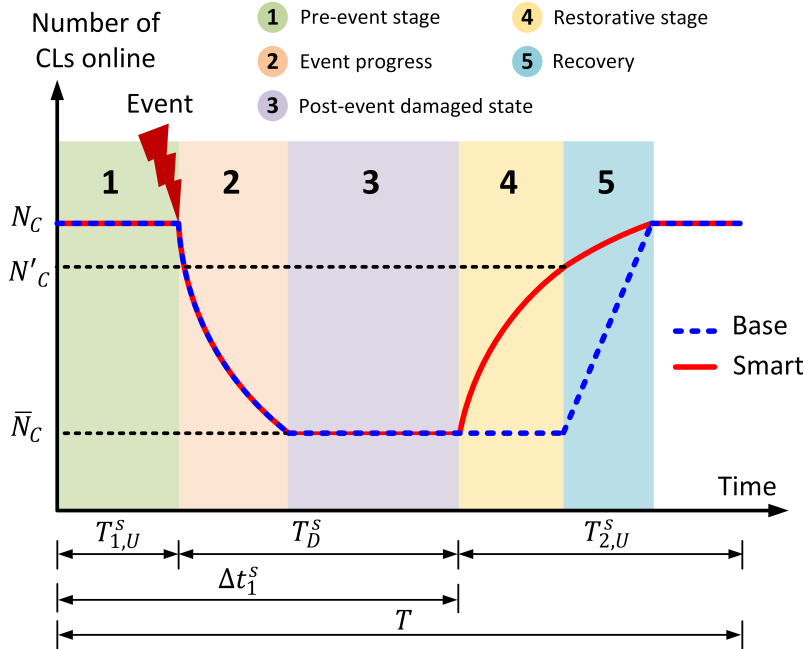


Figure 1: Typical resilience assessment curve based on the number of weighted CL online. The time variables on the x -axis refer to the smart network [26].

The event occurs at the end of $T_{1,U}$ and sustains for a certain time. The time of event progress depends on the nature and intensity of the event and is denoted by phase 2 of the resilience assessment curve. Some CLs get disconnected due to the severity of the event. \bar{N}_C be the number of CLs that remain online after an event occurs. Phase 3 denotes the time for damage assessment. Smart networks have smart devices and damage assessment tools that can decrease the damage assessment time significantly. The CLs get disconnected when an event occurs until the point when repair or restoration starts. This is the downtime for CL and is denoted by T_D . Δt_1 is the period from the initial time to the time when repair/restoration begins. For the base case, the repair does not start until the recovery state, phase 5, whereas for the smart network DGs and remote-controlled switches (RCSs) can assist in load restoration, phase 4. At the point of repair/restoration, some of the CLs become online again and remain online for a time $T_{2,U}$. Let N'_C be the number of CLs that are online after the load restoration phase. The total up and downtime of CL for the entire duration is represented by $T = T_{1,U} + T_D + T_{2,U}$.

In this work, we only consider phases 1 through 4 for quantifying the resilience metric. We will discuss a few parameters that help us define the resilience of a distribution grid as

referred to the critical loads and phases described in Fig. 1. A detailed explanation of these parameters are given in [26] while some of them are modified as necessary for this work.

Availability: Let $i = 1, 2, \dots, N_C$ be the CLs connected in a system, $T_U^i = T_{1,U}^i + T_{2,U}^i$ be the time period when a CL i is connected to system (up time), and T_D^i be the time period when i is disconnected from the system (down time) due to an extreme event. Hence, availability refers to the fraction of time when i is online and is defined as:

$$\mathcal{R}_\psi = \frac{\sum_{i=1}^{N_C} T_U^i}{\sum_{i=1}^{N_C} (T_U^i + T_D^i)} \quad (1)$$

Here, T_U^i and T_D^i for each i depends on the type of network. For smart network, some disconnected CLs are restored in phase 4 which increases the overall availability of the system. Here, the choice of N_C is problem specific and can represent a single customer as well as a particular feeder [26].

Robustness: Let n_0 be the number of CLs that are disconnected from the system at a given time. Then the outage incidence, θ is defined as:

$$\theta = \frac{n_0}{N_C} \quad (2)$$

If $N_C - \bar{N}_C$ be the maximum number of CLs disconnected from the system and θ_{max} is the maximum outage incidence for a given time, then robustness is defined as:

$$\mathcal{R}_\beta = 1 - \theta_{max} = 1 - \frac{N_C - \bar{N}_C}{N_C} = \frac{\bar{N}_C}{N_C} \quad (3)$$

Brittleness: Let D be the percentage of infrastructure damage in the system. For simplicity, we only consider distribution lines as infrastructures in this work. Brittleness is the level of disruption that occurred in the system with respect to damage. For instance, if the damage of a single distribution line affects the entire system then the system is highly brittle. The brittleness of a system with N_C critical loads is defined as:

$$\mathcal{R}_\gamma = 100 \times \frac{\theta_{max}}{D} \quad (4)$$

Resistance: According to [26], a system has higher resistance if it can withstand extreme events better and can operate the loads for a longer period before getting disconnected. With this notion, a resistant system should have better physical infrastructures, proper damage assessment methods, and situational awareness in case of extreme events. Furthermore, the

resistance is also dependent on the nature of the extreme event. Here, σ is the measure of an extreme event and is obtained as described in [26]. Based on the measure of the event and time before which the repair and restoration begins, the resistance of a system is given by:

$$\mathcal{R}_\xi = \frac{\sigma \sum_{i=1}^{N_C} T_{1,U}^i}{\theta_{max} N_C \Delta t_1} \quad (5)$$

Resourcefulness: Let N_{SW} be the number of tie-line switches, N_S be the number of generating sources, and N_P be the number of simple paths from each of the sources to CLs after an event has occurred in a network. Then the available resources are useful only if their existence is meaningful in system restoration. Thus, resourcefulness is defined as:

$$\mathcal{R}_\delta = \frac{N_P}{(N_{SW} + N_S) \times N_C} \quad (6)$$

For the base network, the only available source is the substation so $N_S = 1$ for the base case. For the smart network, N_S increases as the number of DG increases. However, the resourcefulness decreases if those DGs are not utilized in network restoration after the event has occurred which is ensured by N_C . Thus, resourcefulness can be useful for planning the placement and number of DGs to enhance system resilience.

2.1.3.2 Risk Metrics: As discussed in [25], we use $CVaR$ as a risk measure for each of the parameters. VaR is defined as the specific threshold ζ , such that with a specified probability of α VaR does not exceed ζ . On the other hand, $CVaR$ is the expected value of the distribution that exceeds VaR . Both of these metrics depend on the value of α and are commonly represented as VaR_α and $CVaR_\alpha$. If $p(I)$ be the probability distribution of a random weather event I then the cumulative probability distribution that the parameter \mathcal{R} will not exceed ζ when impacted by I is given by:

$$\Psi(\zeta) = \int_{\mathcal{R}(I) \leq \zeta} p(I) dI \quad (7)$$

Thus, VaR_α and $CVaR_\alpha$ are then defined by:

$$VaR_\alpha(\zeta) = \inf\{\zeta \in \mathbb{R} : \psi(\zeta) \geq \alpha\} \quad (8)$$

$$CVaR_\alpha(\zeta) = (1 - \alpha)^{-1} \int_{\mathcal{R}(I) \geq VaR_\alpha} \mathcal{R}(I) p(I) dI \quad (9)$$

$CVaR_\alpha$ represents the value of parameter for the extreme $(1 - \alpha)\%$ of impacts. It is also to be noted that the distribution of parameters below and above the specified threshold ζ represent the complete distribution of extreme events with a probability of α and $1 - \alpha$ respectively.

2.1.3.3 Multi-criteria Decision Making using Choquet Integral: When it is essential to include multiple criteria in a decision making process then a single attribute or performance-based analysis do not accurately justify the decision. The Choquet Integral is an effective method for the MCDM problem [27] and is well suited for our framework.

If μ denote the fuzzy measure on Γ then the discrete Choquet integral of a function $f : \Gamma \rightarrow \mathbb{R}^+$ with respect to μ is defined as [27]:

$$\mathcal{C}_\mu(f) := \sum_{i=1}^n (f(i) - f(i-1))\mu(\{\mathcal{R}_1, \mathcal{R}_2, \dots, \mathcal{R}_n\}) \quad (10)$$

where $f(\cdot)$ are arranged in ascending order of its magnitude and is the $CVaR_\alpha$ of the parameters calculated using (9), $\mu(\mathcal{R}) = \eta_{\mathcal{R}}$ is defined as the Shapely value which accounts for the behavioral analysis of any fuzzy measures, and $f(0) = 0$. More detail information on the Shapely value analysis and fuzzy measures is provided in [28]. Choquet integral gives the overall score of alternative decisions in problem involving multiple parameters for each decision.

2.1.4 Probabilistic Event and Impact Assessment

Fig. 2 shows the overall framework to quantify the system resilience using a stochastic simulation-based approach and is described in detail below. It is to be noted that the smart network contains DG-based restoration and RCS that can improve the damage assessment and restoration phase to enhance the overall resilience of the system.

The extreme wind event and its impact is characterized using its probability distribution and line fragility model. The fragility model of any distribution line gives the outage probability of the line subjected to a particular wind speed and can be represented as:

$$\mathbb{P}_v^l = \begin{cases} \mathbb{F}_n^l & v < v_{cri} \\ \mathbb{P}^l(v) & v_{cri} \leq v < v_{col} \\ 1 & v \geq v_{col} \end{cases} \quad (11)$$

where \mathbb{F}_n^l is the failure rate of line l in normal weather condition, $\mathbb{P}^l(v)$ is the failure probability of line l as a function of v , v_{cri} is the critical wind speed at which line l experiences failure, and v_{col} is the wind speed threshold beyond which line l is guaranteed to fail. Since the process of identifying an event and its impact is purely stochastic, Monte-Carlo simulations are conducted to evaluate the probabilistic impacts of the event on the power distribution grid. The approach is generic as each event is simulated for several trials. The fragility models provide the failure probability of any distribution lines. With the increase in wind intensity,

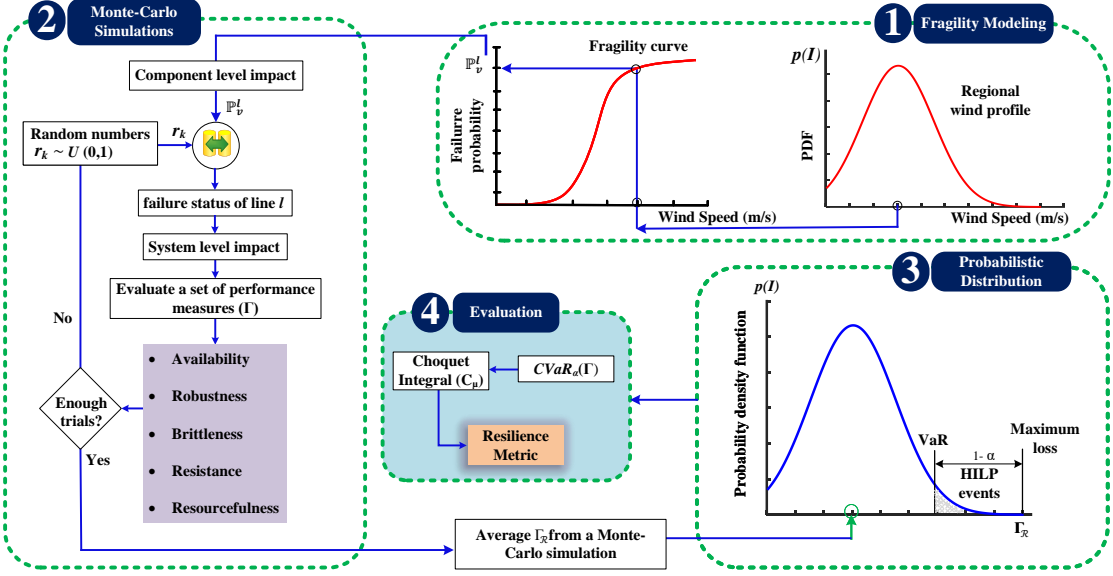


Figure 2: Simulation-based framework for resilience metric computation; Fragility modeling feeds the failure probability to Monte-Carlo simulation. Monte-Carlo simulation calculates the average value of a performance measure for a given event. $CVaR_\alpha$ is then calculated using the pdf of a given extreme event case.

the failure probability increases accordingly. Monte-Carlo simulations help us identify the number of lines being failed in each trial, and resilience-driven parameters are evaluated using (1) – (6). For smart network, the optimization framework using DGs are modeled and simulated as described in [18]. In the optimization model, all the CLs are equally important and a weight factor of 10 is used for CLs and 1 for non-CLs. At the end of each simulation, the average of evaluated parameters for all trials is then mapped with the respective intensity of the events to form a distribution of each parameter corresponding to its intensity.

The probability distribution of each of the parameters corresponds to the distribution of the intensity of the event. Thus, $CVaR_\alpha$ of each of the parameters can be calculated using (9). It is to be noted that the value of α is consistent for each of the parameters. To combine $CVaR_\alpha$ in the decision-making process, the priorities of each of the parameters are obtained from the system operators and Shapely values of those priorities are evaluated. Finally, based on the $CVaR_\alpha$ of each of the parameters and their Shapely values, Choquet Integral gives an overall score using (10). To identify the interaction of each of the parameters, λ is also considered in the overall calculation process. The overall score obtained from Choquet Integral is the resilience metric for the distribution system. The described process is holistic as it considers all of the resilience-driven parameters (both attribute-based and

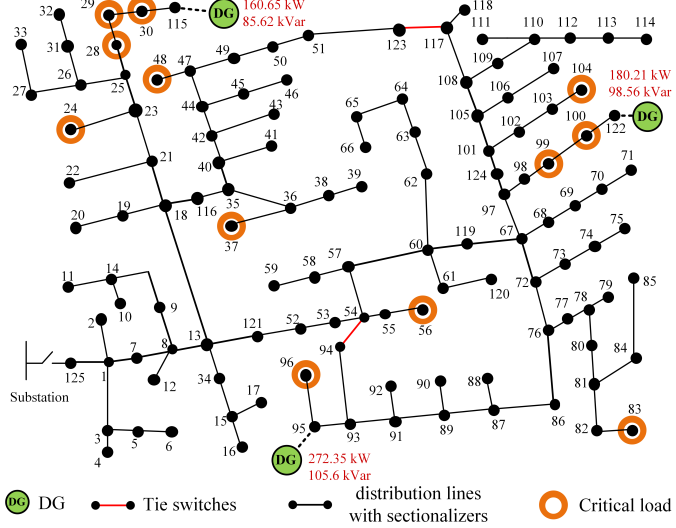


Figure 3: Modified IEEE-123 test case with DGs, tie switches, and CLs.

performance-based) with their priorities in a system along with the associated risk.

2.1.5 Preliminary Research Results

The proposed method of resilience metric quantification using $CVaR_\alpha$ of multiple parameters and Choquet Integral is demonstrated on IEEE 123-bus test system, Fig. 3. The simulation is carried out for extreme wind-related events. It was experimentally verified that 1000 trials are enough to achieve convergence of MCS for any wind speed scenarios.

2.1.5.1 Calculating CVaR of Parameters: The five parameters defined in Section 2.1.3.1 are calculated based on Fig. 1 and using the simulation method described above. Fig. 4 shows the PDF of \mathcal{R}_ψ obtained for each wind speed along with VaR_α and $CVaR_\alpha$ values. For all of the cases, the value of α is set to be 0.95. The VaR_α and the $CVaR_\alpha$ are calculated using (8) and (9). The risk metrics for other parameters are calculated in a similar fashion and are shown in Table 1. Each of the parameters are normalized using min-max normalization technique for generality.

2.1.5.2 Quantifying Resilience using Choquet Integral: To compute the resilience metric based on the multiple parameters and their respective importance, five different cases are developed. For each of the cases, $\mu(\cdot)$ is assigned for each parameter as shown in Table 2.

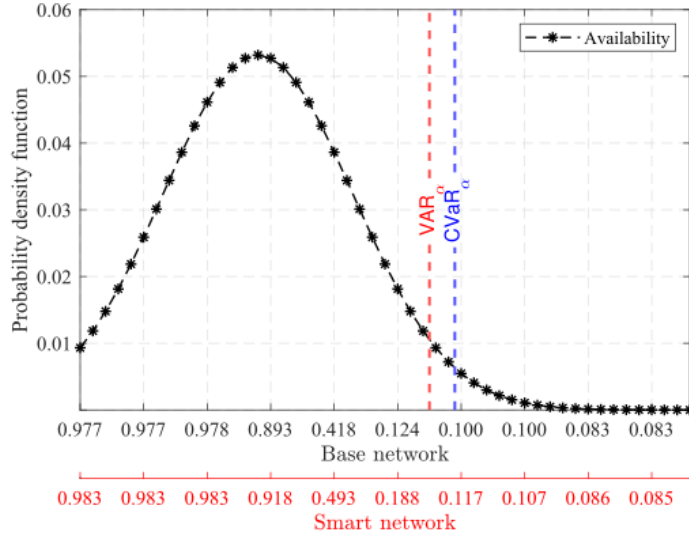


Figure 4: PDF of availability for base and smart network.

Table 1: $CVaR_\alpha$ of normalized resilience-based parameters for base and smart network

Cases	\mathcal{R}_ψ	\mathcal{R}_β	\mathcal{R}_γ	\mathcal{R}_ξ	\mathcal{R}_δ
Base	0.01115	0.00012	0.01656	0.0037	0.00005
Smart	0.01932	0.00012	0.01656	0.0039	0.00314

These are the initial fuzzy weights given by the experts or system operators that indicate the priority of one parameter over others.

Table 3 shows the Shapely value of each of the parameters as obtained from their initial fuzzy weights. These values also indicate the marginal contribution of each of the parameters in the respective cases. For instance, in Case I the importance of \mathcal{R}_ψ and \mathcal{R}_δ are greater than the importance of other parameters. Hence, these two parameters contribute more towards resilience quantification than the others. For different cases, the marginal contribution of each of the parameters differ according to the priority set by the system operator or expert.

The Choquet Integral values for the base and the smart network and each of the cases are shown in Table 4. It can be seen that the resilience of the smart network is always greater than that of the base network regardless of individual test cases due to the presence of DGs. However, the resilience for individual networks varies with the Shapely values of each of the parameters. For instance, if we look at the smart network, Case IV is more resilient than any of the other cases as higher priority is given to load availability and infrastructural

Table 2: Initial fuzzy weights of parameters
for resilience metric calculation

Cases	$\mu(\mathcal{R}_\psi)$	$\mu(\mathcal{R}_\beta)$	$\mu(\mathcal{R}_\gamma)$	$\mu(\mathcal{R}_\xi)$	$\mu(\mathcal{R}_\delta)$
I	0.9	0.25	0.15	0.6	0.85
II	0.6	0.5	0.45	0.5	0.6
III	0.3	0.8	0.85	0.6	0.2
IV	0.9	0.6	0.6	0.6	0.2
V	0.2	0.6	0.6	0.6	0.9

Table 3: Shapely values of each parameters
based of their initial weights.

Cases	$\eta_{\mathcal{R}_\psi}$	$\eta_{\mathcal{R}_\beta}$	$\eta_{\mathcal{R}_\gamma}$	$\eta_{\mathcal{R}_\xi}$	$\eta_{\mathcal{R}_\delta}$
I	0.35235	0.07617	0.04451	0.20400	0.32294
II	0.23225	0.18573	0.16404	0.18573	0.23225
III	0.09441	0.30385	0.33202	0.20849	0.06121
IV	0.34422	0.19903	0.19903	0.19903	0.05869
V	0.05869	0.19903	0.19903	0.19903	0.34422

investments (i.e., \mathcal{R}_β , \mathcal{R}_γ , and \mathcal{R}_ξ). However, this is not true for the base network as loads are not picked up during the restoration phase in the base network making its availability lower than the smart network. It is also interesting to notice that, the resilience for Case I and Case IV does not have a huge difference although for Case I, the priority towards infrastructural investment is less. Hence, the operators can have the flexibility to focus more on less expensive decisions and still enhance the system's resilience.

Table 4: Choquet Integral values based on
Shapely values of each parameters

Network	Case I	Case II	Case III	Case IV	Case V
Base	5.45	6.03	7.36	7.89	4.72
Smart	9.36	8.68	8.36	10.93	6.31

2.2 Risk-based Resilience Planning of Power Distribution Systems

2.2.1 Prior work on Power Distribution Planning and their limitations

The existing literature on power distribution resilience includes numerous articles on operational planning to mitigate or reduce the impact of an imminent threat such as an upcoming storm [29]. Such solutions build resilience via operational response rather than infrastructural upgrades. In operational planning, the decisions are to be made for an upcoming event that is known with a high level of certainty and thus requires considering only a limited number of scenarios for decision-making. On the contrary, long-term planning requires a probabilistic analysis over a wider range of scenarios with a higher level of uncertainty for decisions related to system hardening, infrastructure upgrades, resource allocation, and sizing [30]. These decisions must also connect to the operational problem if and when the events are realized in practice. Thus, the problem is further complicated by additional stages of operational decision-making leading to an explosion of state space to be considered for decision-making.

The related literature on resilience-oriented design and pre-disaster resource allocation usually employ a stochastic programming model to minimize the expected cost of the future operational scenarios [31, 32]. For example, in [31], a heuristic search is employed to identify the optimal restoration path and obtain a resource allocation plan. These solutions, however, consider short-term operational requirements for a known HILP event and are not suitable for infrastructure planning. The related work on resilience-oriented distribution system long-term planning also employs stochastic optimization formulations, including a tri-level robust optimization model [33, 34], and a two-stage stochastic optimization model [35–37]. The tri-level optimization model formulates the resulting problem in a defender-attacker-defender model that is then converted into an equivalent bi-level model and solved using iterative approaches such as CCG or greedy search algorithms [33]. The tri-level approach optimizes for the worst possible outcomes and hence is not suitable for a probabilistic analysis for infrastructure planning that needs to be cost-effective and optimal for a large range of fu-

ture scenarios. Alternatively, the two-stage stochastic programming method considers the overall impact of stochastic fault scenarios in planning decisions rather than just the worst-case scenarios [35, 38]. The existing two-stage stochastic optimization formulations used in resilience-oriented distribution grid design either assume that all scenarios are observed with equal probability or perform the planning based on only a targeted set of scenarios [39–41]. While such methods are generally applicable, other approaches such as importance sampling and stratified sampling techniques can be more effective in representing HILP events and their impact probabilities in the optimization process [42, 43]. These techniques are widely adopted in power systems reliability studies [44, 45]. For a resilience-oriented long-term planning problem, the goal is to determine optimal investments to reduce the consequences (here, customer outages) of the HILP events. Mathematically, this amounts to minimizing the mean of consequences and, more importantly, reducing the tail of the consequence of the HILP events [46].

1. *Risk-averse Two-stage Stochastic Programming for Distribution Grid Resilience*: The two-stage stochastic programming problem is formulated as a MILP problem where Stage-1 decisions are the infrastructure planning decisions optimized to reduce the risks of outages due to HILP events assuming optional operational phase decisions.
2. *Probabilistic scenario generation and smart scenario reduction strategy*: A Monte-Carlo-based probabilistic scenario generation framework and smart scenario selection strategy is proposed to reduce the large scenario samples to representative scenarios.
3. *Trade-off analysis on risk minimization vs. expected loss minimization*: Different case studies are presented to identify the trade-off of adopting risk-neutral vs. risk-averse policies in the planning decisions. The analysis can provide insights into adopting risk-driven solutions when the utmost priority is to maintain an uninterrupted power supply to critical customers during extreme weather events.

2.2.2 Planning Problem Representation

A power distribution network can be graphically represented as $G(V, E)$, where the vertices V represent the buses or nodes while the distribution lines are represented by the edges E . The overall objective of the two-stage framework is to identify the first-stage optimal planning decisions that minimize the expected operational cost in the second stage. In this work, DG siting and sizing are the planning decisions whereas the second stage objective is to minimize the prioritized load loss once a scenario is realized. DGs with grid-forming inverters are assumed in this work. Such grid-forming DGs can be used for intentional islanding when some area of the distribution grid gets disconnected from the system due to an extreme event.

The two-stage objective function is a random variable. Thus, determining the optimal planning decision is the problem of comparing random cost variables as a function of the planning cost and the operational cost. The overall problem is formulated as a risk-averse stochastic optimization problem in which the first stage problem minimizes the cost of planning and the weighted combination of the expected value and the *CVaR* of the second stage problem. The second stage problem is the operational stage that minimizes the total prioritized loss of load for every scenario realization.



Figure 5: Two-stage planning framework example for a specific scenario.

2.2.3 Problem formulation

The resilience-driven distribution system planning problem is formulated as a two-stage stochastic optimization problem where the overall objective function can be defined as:

$$\min(1 - \lambda)\mathbb{E}(Q(\delta, \mathcal{E})) + \lambda CVaR_\alpha(Q(\delta, \mathcal{E})) \quad (12)$$

where,

$$\begin{aligned} \mathbb{E}(Q(\delta, \mathcal{E})) &:= \left(\sum_{\xi \in \mathcal{E}} \sum_{i \in \mathcal{B}_S} \sum_{\phi \in \{a,b,c\}} (1 - s_i^\xi) w_i P_{Li}^{\phi, \xi} \right) \\ CVaR_\alpha(Q(\delta, \mathcal{E})) &:= \left(\eta + \frac{1}{1 - \alpha} \sum_{\xi \in \mathcal{E}} p^\xi \nu^\xi \right) \end{aligned}$$

The problem objective in the first stage is to minimize the weighted sum of expected value and $CVaR_\alpha$ of the second stage cost, represented by $Q(\delta, \mathcal{E})$. To analyze the trade-offs, this formulation has not used minimization of planning cost. Instead, we use a budget constraint and observe the associated trade-offs for risk-averse and risk-neutral decisions when system planners have a limited investment budget. The objective of the second stage of the problem, $Q(\delta, \mathcal{E})$, is to minimize the prioritized load loss or maximize the restoration of prioritized loads for each $\xi \in \mathcal{E}$. The second stage costs correspond to the optimal restoration decisions once a scenario has been realized. Hence, each variable corresponding to the second stage of the problem is scenario-dependent. $P_{Li}^{\phi, \xi}$ represents the active power

demand at node i for phase ϕ and scenario ξ and $s_i^\xi \in 0, 1$ is the load pick-up status variable that determines whether the load at node i is picked up or not. The CLs are prioritized by a weight variable w_i . Since the CLs are critical for any scenario, w_i remains the same for all scenarios. Furthermore, the scenarios have a specific probability, p_ξ , associated with them, which comes from the scenario reduction method discussed before. For the expression $CVaR_\alpha(Q(\delta, \mathcal{E}))$, ν_ξ is an excess variable which ensures that $CVaR_\alpha$ is calculated only for realizations beyond VaR_α for each scenario ξ .

Here, DG location (δ_i^{DG}) and size of the DG (β_i^{DG}) are the first stage decision variables. In this work, the per unit cost for DG installation and sizing is assumed to be the same for each location; these assumptions can be easily relaxed. Constraint (13a) ensures that the total cost of DGs should be between $[\$0, \mathcal{C}_{max}^{DG}]$ regardless of the cost of installation in an individual location. This gives the freedom of utilizing the overall budget for a single big-sized DG or distributing the budget to multiple smaller-sized DGs. Constraint (13a) contains a non-linear term $\delta_i^{DG} \times \beta_i^{DG}$ which is linearized using big-M method as discussed in [47]. Constraint (13b) restricts the DG location variable to binary. The DG location variable δ_i^{DG} is 1 if a DG is located in node i , else 0. Furthermore, constraint (13c) ensures that VaR_α for the distribution of load loss in the second stage is a real number. Furthermore, VaR_α is independent of scenarios and is obtained with the solution of the first stage.

$$\sum_{i \in \mathcal{B}_{DG}} c_i^{DG} \delta_i^{DG} \beta_i^{DG} \leq \mathcal{C}_{max}^{DG} \quad (13a)$$

$$\delta_i^{DG} \in \{0, 1\} \quad (13b)$$

$$\eta \in \mathbb{R} \quad (13c)$$

The overall problem formulation can be summarized as:

Objectives:

- 1) Minimize weighted sum of expected value and $CVaR_\alpha$ of the second stage cost

Constraints:

- 1) First-stage constraints (scenario independent)
- 2) Second-stage constraints (secenario dependent)
 - a) Connectivity constraints
 - a) Three-phase unbalanced power flow constraints
 - c) Network operational constraints
 - d) DG operating constraints
 - e) $CVaR_\alpha$ constraints



Figure 6: Overall architecture of risk-averse two-stage planning problem. The first stage seeks the optimal planning decisions that minimize the expectation and risk of the recourse cost in the second stage for several scenario realizations. The scenarios are generated using Monte-Carlo simulation and reduced based on average loss for each scenario.

2.2.4 Proposed scenario generation and selection approach

The overall architecture of the proposed method is shown in Fig. 19. Only wind-related events are used in this work and the probability distribution of extreme wind events is considered to generate the scenarios. Monte Carlo simulations (MCS) are conducted to identify the impact of probabilistic events, and an appropriate scenario reduction method is implemented to identify representative scenarios. Finally, the planning problem is solved in a two-stage stochastic optimization setting based on a selected number of scenarios.

Fig. 7 shows the event probability distribution for a windfall in three different regions observing extreme, high, and normal wind profiles. The extreme regional wind profile is used to model extreme events in this work. For simplicity, only distribution lines are assumed to be affected by wind in this work. Although wind-related events have spatiotemporal dynamics [48], we assume that for a distribution system, that covers a small region, the wind speed for the entire region is the same. MCS is performed for each wind speed case so as to also include the extreme tail probability events. This process is represented by block 2 in Fig. 19. For each wind speed scenario u , the component level failure probability $p_f(u)$ determines the operational state of a particular component in the distribution grid. Component level fragility curves [15] or prototype curve fit models [49] can be used to model

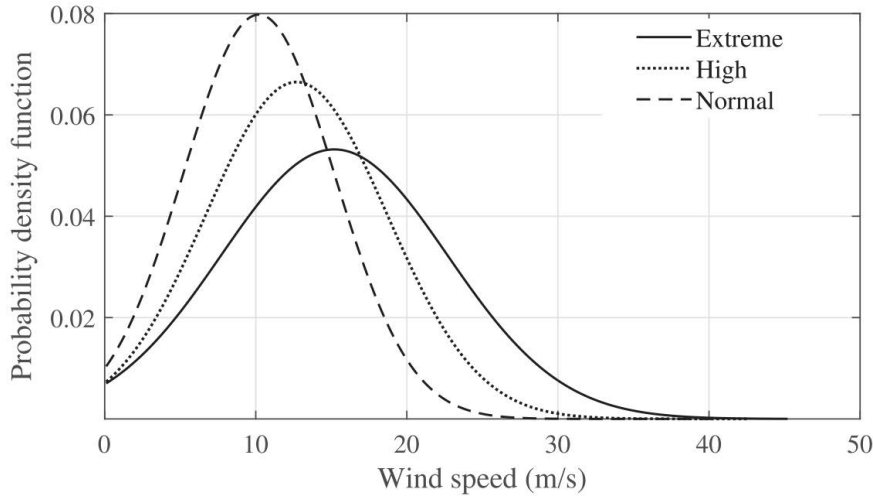


Figure 7: Regional wind profile.

the impacts of extreme events such as hurricanes or other high-speed wind events on power systems. In this work, we have used the component fragility curve that maps the probability of failure of distribution system components conditioned on the intensity of the hazard (e.g., a wind speed). The fragility curve values are randomly selected for simulation purposes; however, if available, empirical data can be used to adjust the parameters [50].

MCS provides an extremely large number of scenarios. One major challenge in any stochastic optimization setting is handling many scenarios within the optimization framework. Furthermore, the solution should be optimal for all scenarios that make the stochastic problem computationally intractable. Existing works use special sampling techniques such as stratified sampling [51] or importance sampling [52] to include the tail probability scenarios in the optimization model appropriately. Distance-based scenario reduction methods have also been used where a probabilistic distance measure is minimized to obtain a reduced scenario distribution that closely represents the overall scenario distribution [53]. We introduce a new approach to scenario reduction inspired by stratified sampling and distance reduction methods. The proposed approach uses stratification to sample representative scenarios for each wind speed and generates a reduced scenario distribution that closely matches the original scenario distribution.

In this work, the overall number of scenarios is reduced by selecting a representative scenario for each wind speed based on the average Monte-Carlo loss. This process is represented by block 3 in Fig. 3. Let N_u be the total discrete wind speeds under consideration, $N_{\xi,u}$ be the number of scenarios obtained from MCS for each wind speed u , and $L_{avg}^u = \mathbb{E}(L_{\xi,u})$ be

the average prioritized load loss in kW corresponding to $N_{\xi,u}$ scenarios. Let $\Xi = N_{\xi,u} \times N_u$ be the total number of scenarios for the entire MCS. Note that we cannot randomly select a subset of these scenarios as it significantly degrades the accuracy of the optimization solutions. Here, we use a unique sampling technique to drastically reduce the number of scenarios while maintaining the representation of the overall scenarios described next. If ξ_u is a representative scenario for all $N_{\xi,u}$ scenarios corresponding to u , then ξ_u is selected such that the prioritized load loss in the system due to ξ_u ($L_{\xi_u}^u$) is the one nearest to L_{avg}^u . In the case of multiple scenarios with losses nearing L_{avg}^u , one of the scenarios is randomly selected as ξ_u from the identical scenario representations. The proposed scenario reduction technique reduces the total number of scenarios to N_u from Ξ such that p_ξ corresponds to the wind speed profile. This smart scenario selection strategy ensures the practical realization of the second stage problem while incorporating HILP events within the scenarios.

2.2.5 Preliminary Research Results

The effectiveness of the proposed risk-based long-term planning model is verified on a modified IEEE 123-bus case, see Fig. 3. To analyze the planning decisions better, we create a new test case upon hardening 15 randomly selected lines, as shown in Fig. 3. The fragility curves of hardened lines are adjusted so that their outage probability for any extreme event is less than the case when they are not hardened. For CLs, $w_i = 10$ whereas, for non-critical loads, $w_i = 1$. Thus the second stage cost reflects the total amount of prioritized loss of load (in kW). The total non-prioritized demand of the system is $P_D = 4485 kW$ and the prioritized demand is $\sum_{i \in \mathcal{V}} w_i P_{Li} = 20775 kW$. This work uses prioritized demand to analyze the results for different cases.

2.2.5.1 Scenario Generation and Reduction Using the wind speed profile for extreme wind events and failure probability of distribution lines, several trials of MCS simulation are conducted for sampled wind speeds [50]. For this experiment, $N_u = 49$ wind speeds are sampled from the wind speed profile and it was experimentally verified that 1000 Monte-Carlo trials are enough to obtain a converged value of prioritized loss of load in the distribution grid corresponding to each u . Fig. 9 shows the moving average of prioritized loss of load for 1000 Monte-Carlo trials for the base case without hardening and with hardening. It can be seen that the value of the loss is fairly converged in 1000 trials for both cases. Since 1000 trials are conducted for each u , $N_{\xi,u} = 1000$. Hence, the total number of scenarios generated through MCS, $\Xi = 49 \times 1000 = 49000$.



Figure 8: Modified IEEE 123-bus test case

Fig. 10 represents the comparison between L_{avg}^u and L_ξ^u for the test case without hardening and with line hardening. The loss due to reduced scenarios is very close to that of the actual representative scenarios for each u . The y-axis on the right represents the value of $|L_{avg}^u - L_\xi^u|$. It can be seen that the maximum difference occurs at $u = 31m/s$ in Fig. 10.a and has a value of about 78 kW which is < 0.5% of total prioritized demand. The difference in their values comes from the fact the L_{avg}^u is obtained by averaging 1000 different realizations of ξ for a specific u whereas L_ξ^u is the prioritized load loss for a specific failure scenario ξ corresponding the same u . Furthermore, it should be noted that HILP events (tail events) are also sampled in this reduction method which makes this approach highly suitable for resilience planning problems.

2.2.5.2 Risk-based Planning In this long-term planning problem, 6 DG locations are pre-selected as potential locations for the placement of DG units. The selected potential DG locations are nodes 95, 122, 39, 85, 56, and 66. However, the DG locations are decided by the optimization model and $\delta_i^{DG} = 1$ if and only if $\beta_i^{DG} > 0$. From the operator's perspective, it is often practical to have a limited budget while planning the siting and sizing strategies

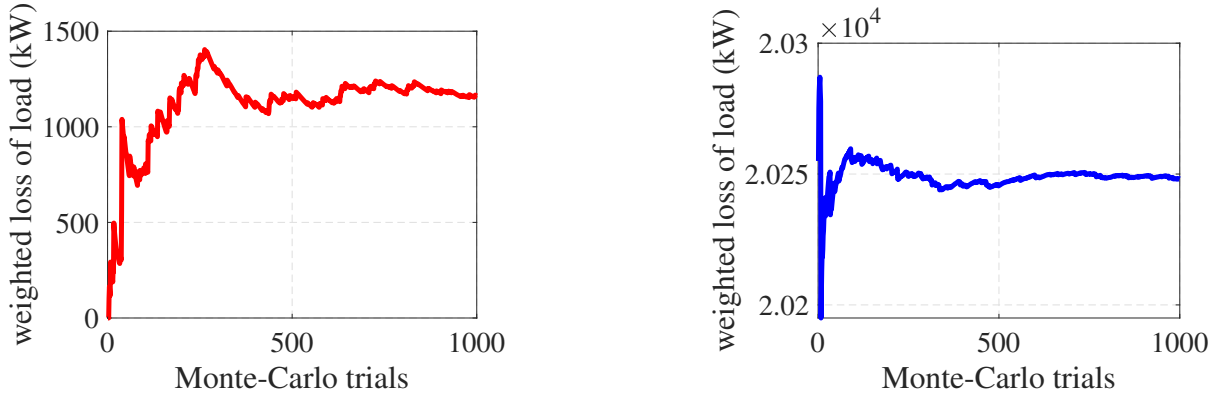


Figure 9: Moving average of loss of load obtained for 1000 Monte-Carlo trials a) without hardening when $u = 15 \text{ m/s}$ and $p_f(u) = 0.002$ and b) with line hardening when $u = 40 \text{ m/s}$ and $p_f(u) = 0.915$. For each wind speed scenario, it can be guaranteed that the prioritized load loss converges after 1000 Monte-Carlo trials.

Table 5: Base case expected value and $CVaR_\alpha$ of prioritized load loss.

line hardening	$\mathbb{E}(Q(\delta, \mathcal{E}))$ in kW	$CVaR_\alpha(Q(\delta, \mathcal{E}))$ in kW
No	5982.57	20601.58
Yes	4541.76	19839.39

for DGs. The total budget is constrained so that the sum of the DG units is less than or equal to 900 kW. For risk-driven problems, α is set at 0.95, meaning that 5% tail scenarios (HILP) are considered to have greater risks.

To identify the trade-off among different DG-based planning strategies, 6 locations — 39, 56, 66, 85, 95, and 122 — are selected as potential DG locations. First, we discuss the results for the risk-neutral case ($\lambda = 0$). The existing resilience-based planning methods, [39–41], are focused on the risk-neutral case and used as a comparison for this work. The overall capacity of each of the DGs is shown in Table 6. For risk-neutral planning without line hardening measures, no DGs are required to be placed on nodes 36 and 95. However, for mean-risk and risk-averse situations, the planning strategies change significantly. For risk-involved strategies, it is required to place DGs on nodes 39 and 95 while reducing the DG sizes for the rest of the nodes as shown in Table 6. Hence, the trade-off of including risk minimization in the objective is to increase the number of DG units in the system. This can be fruitful for extreme event scenarios when picking up some of the CLs is required, even though it increases the expected value of prioritized load loss. Table 6 also shows the



Figure 10: Comparison of prioritized load loss obtained for two sets of reduced scenarios a) without hardening b) with hardening.

expected value and $CVaR_\alpha$ of prioritized CLs picked up by different planning strategies. It can be seen that the expected value of prioritized CLs picked up does not change much regardless of the risk preference. However, for risk-based strategies (both mean risk and risk-averse), $CVaR_\alpha$ of prioritized CLs picked up increases by 200 kW compared to the risk-neutral case.

The effect of risk aversion is even more pronounced in the case with the line-hardening strategy. Fig. 11 shows a restoration and planning solution for a specific scenario of HILP nature, $u = 28 \text{ m/s}$. The lines and nodes with black color are the energized section, whereas non-energized sections are represented by gray. Similarly, red lines represent out-of-service lines due to the particular outage scenario. Similar to the restoration for cases without line hardening measures, the risk-neutral solution does not include DGs in nodes 39 and 95. When the objective is risk-neutral ($\lambda = 0$) some of the prioritized critical loads are not picked up in this specific scenario as picking up critical loads in this scenario would not affect the expected value of load served for the overall scenarios. Since the objective is to minimize the expected value of prioritized load loss for entire scenarios, DG at location 95 is not selected. Note that the probability of HILP scenarios is low. Since the expected value contains the product of this probability with the objective function in the restoration phase, the net value is significantly low to affect the overall expected value. However, when the objective is risk-averse, any prioritized load that the nearest possible DG can pick up is given the top priority for any HILP event. For instance, it can be seen that load at node 62 is picked up by DG at node 95 through path 95-93-94-54-57-60-62. Hence, this draws an important conclusion that risk-averse decisions enhance long-term resilience planning by focusing the extreme HILP events.

Table 6: Expected value and $CVaR_\alpha$ of prioritized load loss and prioritized critical load (PCL) picked up for different values of λ . The DG planning strategy differs along with the risk preference defined by λ . All of the values mentioned here are in kW.

	WITHOUT LINE HARDENING						WITH LINE HARDENING							
	Existing methods [39–41]			Proposed method			Existing methods [39–41]			Proposed method				
	$\lambda = 0$		$\lambda = 0.5$	$\lambda = 1$	$\lambda = 0$		$\lambda = 0.5$	$\lambda = 1$	$\lambda = 0$		$\lambda = 0.5$	$\lambda = 1$		
$\mathbb{E}(Q(\delta, \mathcal{E}))$	3567.12			3586.28			3595.51			2467.46				
$CVaR_\alpha(Q(\delta, \mathcal{E}))$	19093.89			18885.92			18885.92			18415.04				
Expectation of PCL picked up	15043.93			15016.64			15006.62			16065.76				
$CVaR_\alpha$ of PCL picked up	3406.59			3603.06			3603.06			4953.65				
DG planning strategies	β_{39}^{DG}	β_{56}^{DG}	β_{66}^{DG}	β_{39}^{DG}	β_{56}^{DG}	β_{66}^{DG}	β_{39}^{DG}	β_{56}^{DG}	β_{66}^{DG}	β_{39}^{DG}	β_{56}^{DG}	β_{66}^{DG}		
	0	20	370	20	20	340	20	20	370	0	350	330		
	β_{85}^{DG}	β_{95}^{DG}	β_{122}^{DG}	β_{85}^{DG}	β_{95}^{DG}	β_{122}^{DG}	β_{85}^{DG}	β_{95}^{DG}	β_{122}^{DG}	β_{85}^{DG}	β_{95}^{DG}	β_{122}^{DG}		
	390	0	120	100	300	120	100	270	120	100	0	120		
										100	305	0		
										100	280	0		

Contrary to the existing methods in [39–41], the prioritized CLs have a high chance of being picked up when an HILP event is realized by including risk minimization in the objective. However, when attempting to minimize the risk-averse objective (i.e., the $CVaR_\alpha$), we incur an additional DG cost in the overall planning budget to meet the requirements for risk-averse planning. Thus, through the proposed approach and by including $CVaR_\alpha$ minimization in the objective function, prioritized critical loads can be properly restored in case of HILP events. Furthermore, with the changing trade-off between the expectation and the $CVaR_\alpha$ of the prioritized load loss, the expected value *generally* decreases with the increase in λ .

2.2.5.3 Sensitivity Analysis The value of $CVaR$ depends on several factors such as investment decisions, budget, risk preference, and scenarios under consideration. Here, we present a few of the sensitivity analyses and discuss their impacts on $CVaR$. For simplicity, the analyses are performed only on the system with additional hardening measures already in place and for sensitivity based on time complexity, the analysis is done in terms of expected value of the second stage.

2.2.5.4 Change in confidence level The risk parameters α and λ can affect the planning decisions. The value of $CVaR_\alpha$ highly depends on α as it defines the number of scenarios to be considered in defining the risk. In other words, α can also be defined as risk percentage. For a higher value of α , the value of VAR_α increases, and hence, $CVaR_\alpha$ represents the



Figure 11: DG sizing and siting solution for a specific scenario with additional hardening measures for a) risk-neutral and b) risk-averse planning strategy.

scenarios that create greater losses in the system. Similarly, for a smaller α , $CVaR_\alpha$ incorporates a larger number of scenarios with lower losses in risk quantification. Furthermore, as discussed above, an increasing value of λ denotes an increase in risk aversion towards planning decisions. Fig. 12 shows the relation of $CVaR_\alpha$ for the prioritized loss of load for different values of λ and α . As discussed, $CVaR_\alpha$ decreases when more scenarios are considered as risky (characterized by α). Furthermore, for a fixed α , $CVaR_\alpha$ decreases with the increase in the value of λ as more importance are given to risk minimization. Appropriate values for α and λ need to be selected based on planners' risk aversion criteria.

2.2.5.5 Change in investment strategies Changing investment strategies and allocating the budget properly can also affect the overall planning cost. First, the overall budget for DG sizing and installation is increased so that \mathcal{C}_{max}^{DG} corresponds to $P_{DG}^{max} = 1500 \text{ kW}$ for the same set of DGs and their potential locations. Secondly, 3 additional DG locations (47, 27, and 114) are identified as potential DG placement locations. Fig. 13 shows the distribution of prioritized loss of load when different DG planning measures are taken for risk-neutral and risk-averse cases, respectively. It is interesting to notice that increasing the budget to increase the capacity of DGs has a limited effect on the $CVaR_\alpha$ minimization. However, the expected value of prioritized load loss decreases to 2222.43 kW from 2467.46 kW. The conclusion is consistent for the risk-averse case. However, increasing the number of potential

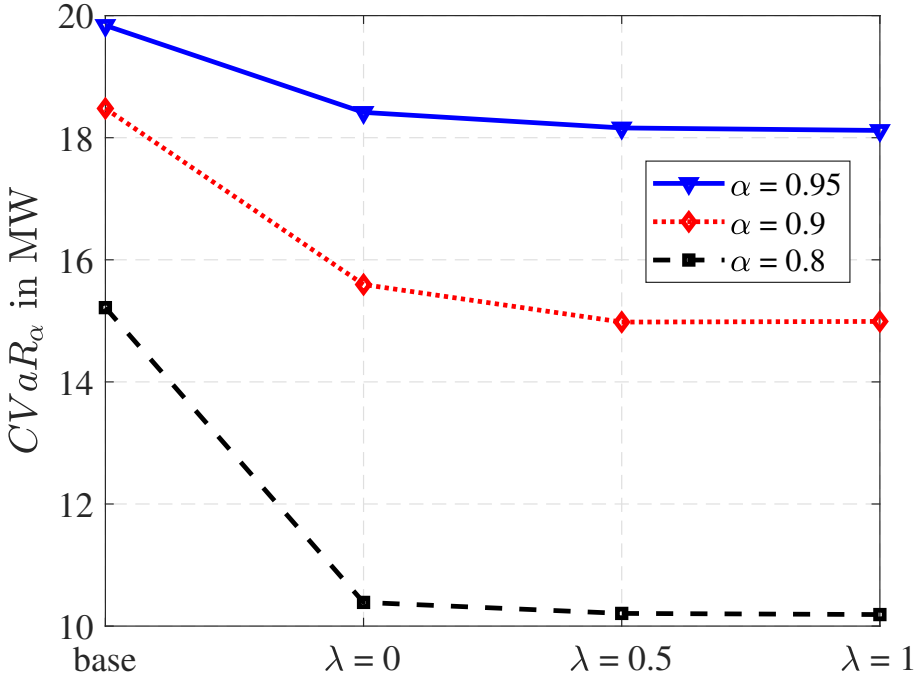


Figure 12: Comparison of $CVaR_\alpha$ of prioritized loss of load for different values of α and risk preference.

DG locations led to significant improvement in $CVaR_\alpha$ minimization. The change in expected loss is, however, insignificant. For the case with 9 potential DG locations, the value of $CVaR_\alpha$ decreases from 18415.04 kW to 16385.51 kW, for the risk-neutral case, and from 18119.1 kW to 15811.59 kW, for the risk-averse case. Thus, with a limited budget, multiple DG sites with smaller DGs are more effective in improving resilience.

2.2.5.6 Change in number of scenarios and set of scenarios Fig. 14 shows five case studies simulated to evaluate the impacts of the number of scenarios (used in optimization) on solution quality and solve time; (a) 7 scenarios, (b) 21 scenarios, (c) 49 scenarios, (d) 98 scenarios, (e) 147 scenarios. Hence, for each case, different scenario sets are obtained using the method discussed in Algorithm 1. Fig. 15 shows the objective function value for the different number of scenarios (used in the optimization problem) along with the corresponding solve times. The result for each case is obtained by taking an average of 10 representative scenario sets closest to the average representative scenario. We can clearly observe the trade-off between the number of scenarios, solution quality, and solve time.

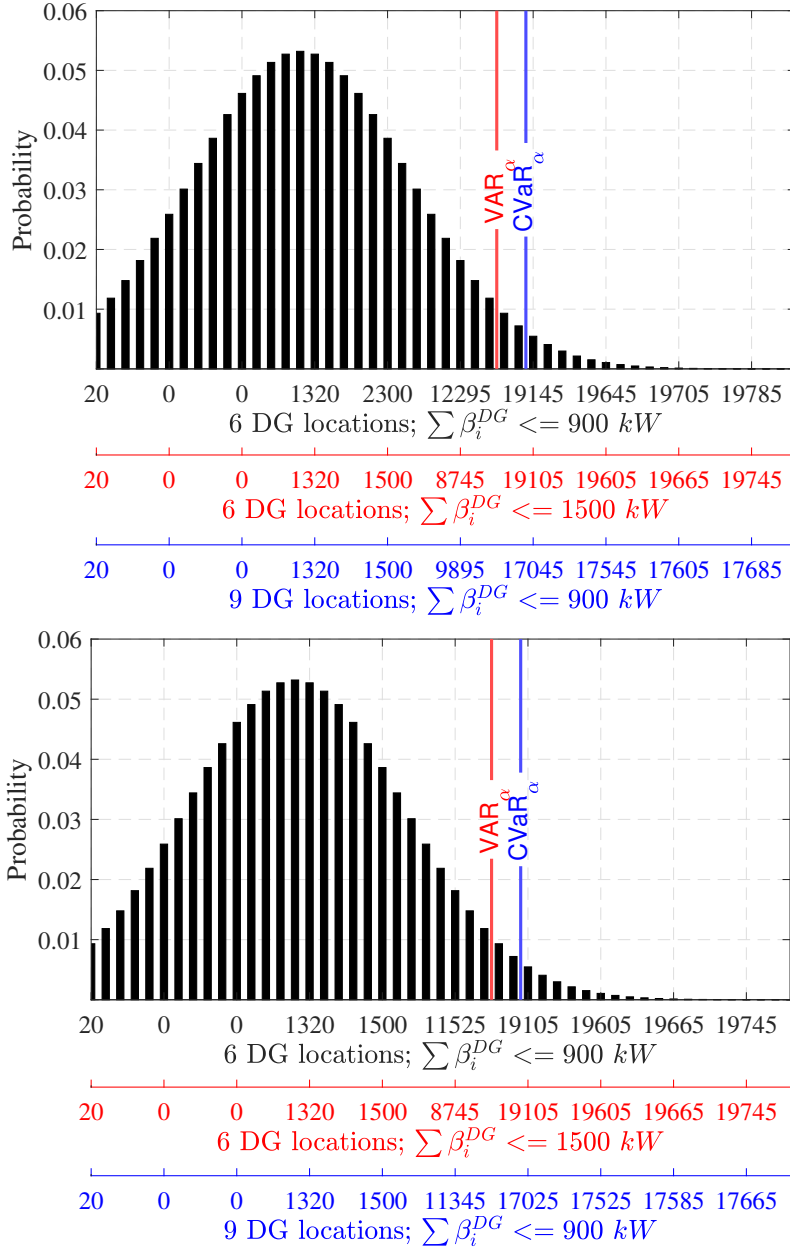


Figure 13: $CVaR_{\alpha}$ for different DG investment strategies for a) risk-neutral and b) risk-averse planning. The value on the x-axis represents the prioritized loss of load for each ξ with corresponding p_{ξ} represented on the y-axis.

When a higher number of scenarios are used in optimization, the solution quality improves; however, it also leads to a significant increase in the solve time. It is also interesting to note



Figure 14: Different number of scenarios with respective probabilities of occurrence: (a) 7 scenarios, (b) 21 scenarios; (c) 49 scenarios, (d) 98 scenarios e) 147 scenarios.



Figure 15: Comparison of objective value and solve time for a different number of scenarios.

that the solution obtained for 49 scenarios (2719.17 kW) is very close to the one obtained for 147 scenarios (2764.16 kW). However, the solve time for the problem with 147 scenarios is 11 times greater than that with 49 scenarios. Hence, 49 scenarios work well from the point of view of solution as well as solve time as the additional number of scenarios increases the computational complexity with no significant improvement in the objective value.

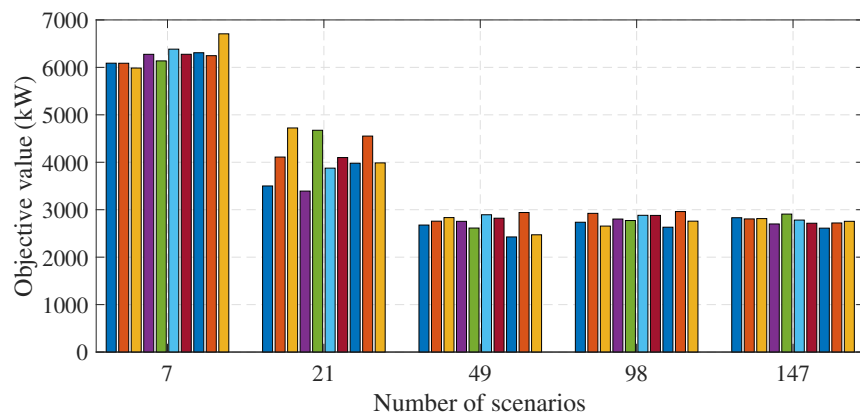


Figure 16: Comparison of objective value on a different set of scenarios for each number of scenarios sampled.

Table 7: 95% confidence interval of the solution obtained using different scenario sets for each number of scenarios.

Number of scenarios	95% CI (kW)	Average objective value (kW)
7	[6105.95, 6393.99]	6249.57
21	[3764.35, 4414.53]	4089.44
49	[2596.13, 2842.21]	2719.17
98	[2721.20, 2879.54]	2800.37
147	[2705.10, 2823.21]	2764.16

3 Spatiotemporal impact assessment of hurricanes and storm surges in electric power systems

3.1 Prior work on extreme weather impact assessment on power systems and their limitations

Several existing works model the impacts of hurricanes on the power grid due to high-speed winds [54]. To model the spatial nature of the event, other works divided the entire power grid into zones such that each zone experiences a different wind speed [55]. However, based on the hurricane's trajectory, each component is impacted differently as the hurricane moves inland, rendering the simplified hurricane model inaccurate for grid impact assessment. Other works model the effect of hurricanes on distribution grid [56]. Since the overall spatial exposure of a hurricane is greater than an entire distribution grid for each time step, the analysis based on the distribution system alone would not be meaningful enough. Furthermore, none of these works model the impact of storm surges on the power grid. In [57], a power system impact assessment framework is presented to identify potential mitigation strategies and enhance resilience against floods. A stochastic optimization framework for substation hardening against storm surge is presented in [58]. [59] evaluated the impacts of tropical cyclones and heatwaves on the power grid. The existing work, however, lacks the spatiotemporal impacts analysis of hurricanes characterizing the compound effects of high-speed wind and flooding.

3.2 Proposed Approach and Modeling

This work aims to develop a compound spatiotemporal effect of hurricanes and storm surges on electric power systems. First, dynamic hurricane scenarios are generated based on historical hurricane tracks and storm surge scenarios are obtained based on the obtained hurricane parameters closer to the landfall. Next, sequential Monte Carlo simulation (MCS) is performed for probabilistic tracks and flooding scenarios for each time step as the hurricane moves inland. Finally, we quantify the impacts using a spatiotemporal loss metric based on the compound effect of hurricanes and floods.

3.2.1 Hurricane Wind field Model

A part of the impact of hurricanes originates from their wind speed. This wind speed is a vector field centered around the hurricane's eye and changes as it moves inland. This wind



Figure 17: Static gradient wind field of a typical hurricane.

field can be modeled as an equation with three variables: v_{max} , $R_{v_{max}}$, and R_s [60, 61]. Here, v_{max} measures the maximum sustained wind speed of the hurricane in knots, $R_{v_{max}}$ measures the distance to v_{max} in nautical miles (nmi), and R_s measures the radius of the hurricane from the hurricane's eye, also known as the radius of the outermost closest isobar (roci), in nmi. Fig. 17 demonstrates the relationship between the wind speed and the distance from the hurricane's eye, and the piecewise mathematical function that represents Fig. 17 is shown in (14).

$$v(x) = \begin{cases} K \times v_{max}(1 - \exp[-\Psi x]) & 0 \leq x < R_{v_{max}} \\ v_{max} \exp[-\Lambda(x - R_{v_{max}})] & R_{v_{max}} \leq x \leq R_s \\ 0 & x > R_s \end{cases} \quad (14)$$

$$\Psi = \frac{1}{R_{v_{max}}} \ln \left(\frac{K}{K-1} \right), K > 1; \quad \Lambda = \frac{\ln \beta}{R_s - R_{v_{max}}}$$

K is a known hurricane constant, x is the distance from the hurricane eye, and β is the factor that the maximum sustained wind speed will decrease at the hurricane's boundary (R_s). Using this equation, it can be assumed that the hurricane has no effect outside this boundary.

To ensure a realistic hurricane wind field, the wind parameters in (14) are obtained using the International Best Track Archive for Climate Stewardship (IBTrACS). IBTrACS

is a global collection of tropical cyclones that merges data from multiple agencies to create a database for historical hurricane parameters at various time steps [62]. The hurricane wind field is generated for each time step t by obtaining $\{R_{v_{max}}^t, R_s^t, v_{max}^t\}$ from IBTrACS and using Eq. (14). The problem of missing data is often possible when using historical data of higher resolution. IBTrACS, however, has approximated values of wind speed at each specified time interval. The work in [60] argues that the individual elements in $\{R_{v_{max}}^t, R_s^t, v_{max}^t\}$ are highly uncorrelated and hence one can randomly sample the corresponding element to approximate the behavior of the hurricane at that particular instance. Hence, for such situations, we have randomly sampled one of the parameters whenever required. The distribution of three of these parameters for historical hurricanes from 1851 – 2012 is shown in Fig. 18.

3.2.2 Storm Surge Model

In this work, we use SLOSH (Sea, Lake, and Overland Surge from Hurricanes) model to generate probabilistic storm surge scenarios. SLOSH is a numerical storm surge model that provides surge heights around the coastal regions from historical or hypothetical hurricanes based on parameters such as atmospheric pressure, hurricane tracks, forward speed, and so forth [63]. It was developed by National Oceanic and Atmospheric Administration (NOAA) and is currently being used by several federal agencies, including the national hurricane center (NHC) and the federal emergency management agency (FEMA), for flood advisories and evacuation. Furthermore, NHC provides a SLOSH Display Package (SDP) tool in which users can generate flooding scenarios based on the direction, forward speed, and intensity of the hurricane followed by the sea tide level [64]. The provided surge heights are above the elevation referenced in the North American Vertical Datum of 1988 (NAV88). The tool also has an added functionality to subtract land elevations so that the surge level is referenced above the ground level. Details on the SDP tool and other surge-related products from NOAA can be found at [64].

SDP contains several coastal basins on which surge scenarios can be created. Furthermore, SDP provides two different surge analyses based on hurricane simulations: Maximum Envelope of Water (MEOW) and Maximum of the MEOWs (MOM). The MEOWs reflect the worst-case snapshots of the storm surge for hurricanes of particular intensity and forward direction but with different landfall locations. This work uses MEOW for storm surge scenarios to identify potential flooding locations. The MEOW scenarios from SDP provide the inundation level for each defined grid in a basin. Let $\mathcal{X}_{\mathcal{S}}$ be the geographical coordinate of

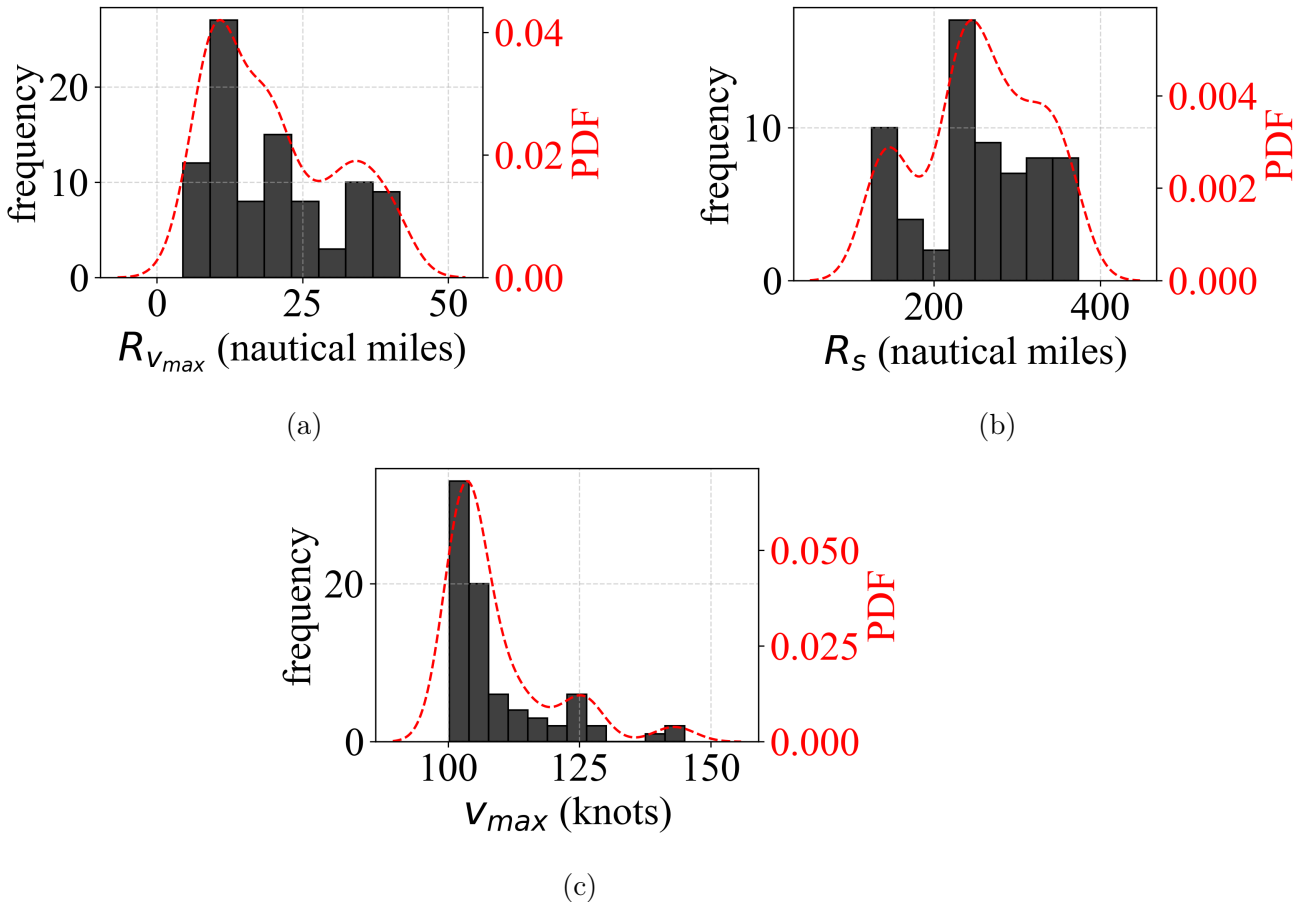


Figure 18: KDE of a) $R_{v_{max}}$, b) R_s , and c) v_{max} estimated from the actual hurricanes that occurred in the USA (1851–2012).

a substation \mathcal{S} . Then, we define $\mathcal{X}_{\mathcal{S},h}^{\mathcal{B}}$ as the inundation level, h , for substation \mathcal{S} situated at \mathcal{X} for basin \mathcal{B} . Since the inundation level is spatially distributed, the expected value of inundation around 0.5 miles of $\mathcal{X}_{\mathcal{S}}$ is assumed to be $\mathcal{X}_{\mathcal{S},h}^{\mathcal{B}}$.

3.2.3 Impact Model

Combined, the hurricane and storm surge creates a spatiotemporal effect on the power grid. The spatiotemporal impact of hurricanes on the power grid is generally guided by the fragility curves of the transmission lines [65]. Let $\Gamma_l^{t,\zeta}$ be the maximum wind speed on line l at time step t due to a hurricane traversing in track ζ . Then the outage probability of line l at time step t due to a hurricane traversing in track ζ is given by (15)

$$\mathbb{P}_{out}^{t,\zeta}(l) = \begin{cases} 0 & \Gamma_l^{t,\zeta} < v_{cri} \\ \frac{\Gamma_l^{t,\zeta} - v_{cri}}{v_{col} - v_{cri}} & v_{cri} \leq \Gamma_l^{t,\zeta} < v_{col} \\ 1 & \Gamma_l^{t,\zeta} \geq v_{col} \end{cases} \quad (15)$$

where $v_{cri} = 48.59$ knots and $v_{col} = 106.91$ knots are the critical wind speed beyond which a transmission line is affected by the hurricane and the wind speed at which the transmission line collapses, respectively [61]. If $\delta_l^{t,\zeta} \in \{0, 1\}$ denotes the line status of line l at time t for hurricane in track ζ , then $\delta_l^{t+1,\zeta} \leq \delta_l^{t,\zeta}$. This ensures that if a line l experiences an outage at time t , it remains out of service for the remaining duration of the hurricane.

The impact assessment from storm surges can be modeled similarly by defining the outage probability of substations. Although FEMA has provided a general fragility level for substations in their HAZUS tool [66], we relax the curve through Weibull stretched exponential function as the substations around coasts have some hardening measures already in place. Hence, the outage probability of a substation \mathcal{S} for a given inundation level h at each basin \mathcal{B} is given by (16)

$$\mathbb{P}_{out}^{\mathcal{S}}(\mathcal{X}_{\mathcal{S},h}^{\mathcal{B}}) = 1 - \exp \left[- \left(\frac{\mathcal{X}_{\mathcal{S},h}^{\mathcal{B}}}{a} \right)^b \right] \quad (16)$$

where $a \in \mathbb{R}^+$ and $b > 2$ are known constants and determine the shape of the fragility curve. When a substation is flooded and deemed out-of-service, all transmission lines connected to and from the substation are disconnected. If $\delta_{l,\mathcal{S}}^{t,\zeta} \in \{0, 1\}$ denotes the line status of line l connected to substation \mathcal{S} at time t for hurricane in track ζ , then $\delta_{l,\mathcal{S}}^{t+1,\zeta} \leq \delta_{l,\mathcal{S}}^{t,\zeta}$. This ensures that if a line l experiences an outage at time t due to a storm surge, it remains out of service for the remaining event duration. When simulating storm surges as an effect of hurricanes, it is important to avoid the redundancy of impact that both transmission line and substation outages can have on the power grid. Let $\mathcal{L}_{\mathcal{H}}^t$ be the set of lines affected by hurricanes and $\mathcal{L}_{\mathcal{S}}^t$ be the set of lines out of service due to a flooded substation at time t . Then, the total number of lines affected by the compound effect of the hurricane and substations inundation due to storm surge is given by $\mathcal{L}_{\mathcal{H}}^t \cup \mathcal{L}_{\mathcal{S}}^t$.

3.3 Event Generation and Impact Assessment Framework

Fig. 19 shows the overall architecture of the event generation and impact assessment process. First, synthetic hurricane tracks were generated based on historical data from IBTrACS. The hurricane impact model is then used to obtain the wind speed experienced by each



Figure 19: Overall architecture for generating hurricane and storm surge scenarios and grid impact assessment.

transmission line. Similarly, flooding scenarios are obtained from SLOSH basins for the given characteristic of the hurricane. The fragility function defined in (15) and (16) provides the outage probability of transmission lines due to hurricanes and the outage probability of substations due to coastal flood inundation. Finally, Monte Carlo simulations (MCS) are conducted to obtain the probabilistic loss for the system. All flood scenarios are considered equally likely. The final spatiotemporal system-level loss metric for each time step is the obtained. The loss metric is the expected value of the loss obtained for the hurricane track and the flood basin for that particular time step.



Figure 20: Hurricane Harvey track and other synthetic tracks obtained from CLIMADA [67].

3.3.1 Hurricane and Storm Surge Scenario Generation

The geographical data and parameters are obtained for Hurricane Harvey, that hit the coast of Texas in August 2017 using IBTrACS. Synthetic hurricane tracks are obtained by perturbing several characteristics of Hurricane Harvey, such as a shift in the initial point of origin, the amplitude of translational speed, bearing angle, landfall decay, etc. The synthetic tracks are obtained from the Climate adaptation (CLIMADA) tool. CLIMADA is a probabilistic natural catastrophe damage model that facilitates climate-based simulations [67]. CLIMADA can generate synthetic tracks in IBTrACS format based on the above perturbations. To synchronize the time steps for the entire duration of the hurricanes, the data is observed every two hours, and the hurricane wind field is generated for each t using (14). Fig. 20 shows the synthetic tracks generated from CLIMADA, and the track with a solid line represents the actual track of Hurricane Harvey from IBTrACS. NOAA predicts that 7 out of 10 times, the estimated hurricane track is within the cone of uncertainty [68]. Hence, five synthetic tracks are selected to be within the cone of uncertainty when forecasted over 120 hours of landfall, i.e., within 240 nmi as per [68].

For storm surge assessment, five different Texas basins are selected; $\mathcal{B} \in \{\text{Matagorda, Corpus, Galveston, Laguna, Sabine}\}$. MEOW scenarios are obtained for all five basins for category 4 hurricanes moving in the northwest direction with a translational speed of 10-15 miles per hour and mean to high tide conditions. One major drawback of using MEOW maps is they are snapshots of the storm surge and carry no time information. However, we

can assume that the components are not inundated until the hurricane approaches. Hence, we assign an activation flag for each component per basin at each time step.

3.3.2 Power Systems Impact Assessment

This work uses a synthetic 2000-bus Texas power grid model to identify the compound probabilistic impact of hurricane and storm surges on the power grid [69]. The grid model maps the synthetic buses, substations, and transmission lines on the geographical footprint of Texas. There are 1250 substations and 1918 transmission lines at 4 different voltage levels — 115 kV, 161 kV, 230 kV, and 500 kV. The total generation capacity of the system is 96291.5 megawatts (MW), and there are 1125 load units with a total size of 67109.2 MW. When the hurricane moves inland, $\Gamma_l^{t,\zeta}$ is obtained for each l and $\mathcal{X}_{\mathcal{S},h}^{\mathcal{B}}$ is obtained for each \mathcal{S} from the MEOW maps. It is assumed that all substations at the coast are elevated at a level of 3 ft from the ground level. Fig. 21 shows the wind field of Hurricane Harvey and MEOW maps on five different basins on the footprint of Texas.

For each ζ , \mathcal{B} , and t , MCS is performed for several trials. For each trial, $\mathbb{P}_{out}^{t,\zeta}(l)$ and $\mathbb{P}_{out}^{\mathcal{B}}(\mathcal{X}_{\mathcal{S},h}^{\mathcal{B}})$ is compared with a uniform random number, $r \sim U(0, 1)$, to identify $\mathcal{L}_{\mathcal{H}}^t \cup \mathcal{L}_{\mathcal{S}}^t$. As discussed before, MEOW maps are time-independent. However, we define an activation flag $\mathcal{S}_{\mathcal{B},h}^{t,\zeta} \in \{0, 1\}$ such that $\mathcal{S}_{\mathcal{B},h}^{t,\zeta} = 1$ makes the substation \mathcal{S} inundated with depth h above the ground elevation for hurricane track ζ , SLOSH basin \mathcal{B} , and time t . In this work, we do not model any drainage system, and hence it is assumed that for future time steps $t + 1$ the inundation level is the same. The objective here is to identify the time stamp when the substation gets flooded to analyze the compound spatiotemporal impact of two different hazards at that time step. The information, $\mathcal{L}_{\mathcal{H}}^t \cup \mathcal{L}_{\mathcal{S}}^t$, is then sent to the power grid simulator to remove the respective branches from the system. Finally, the loss for the particular t is observed as the total load disconnected from the main grid. The MCS trial is conducted until the loss converges to some value.

We assume that the inundation scenarios for each \mathcal{B} and each of the hurricane tracks ζ are equally likely. If N_{ζ} is the total number of tracks under consideration and $N_{\mathcal{B}}$ is the total number of basins, then the system level load loss at each time step t is given by (17)

$$loss_t = \frac{1}{N_{\zeta} \times N_{\mathcal{B}}} \sum_{\zeta=1}^{N_{\zeta}} \sum_{\mathcal{B}} loss_{\mathcal{B}}^{t,\zeta} \quad (17)$$



Figure 21: a) Wind field of Hurricane Harvey and b) Substation flooding scenario, above ground level, for Texas basins.

3.4 Preliminary Research Results

The hurricane data is obtained from IBTrACS [62], and synthetic hurricanes are generated using CLIMADA [67] in Python. SDP [64] is used to obtain the MEOW maps for Texas basins. The power grid is modeled in MATPOWER 7.1 [70], and MCS on the power grid model is conducted in MATLAB R2021a. From the IBTrACS, the hurricane's initial location is in the North Atlantic Ocean, which is observed at “2017 – 08 – 16 06 : 00 : 00” and hence creates no impact on the power grid. Thus, the simulation for the impact assessment begins at the 100th time step, i.e., at the advisory of “2017 – 08 – 24 12 : 00 : 00”. To

avoid any confusion, this timestamp is referred to as $t = 0$ hours for the rest of the paper. Fig. 22a shows the outage probability of a set of transmission lines due to the original Hurricane Harvey track. It can be observed that with the moving nature and intensity of the hurricane, the outage probability of each line changes. The probability is maximum when the line experiences wind speed closer to v_{col} and gradually decreases as the hurricane decays while moving inland. Fig. 22b represents the outage probability of substations for five different Texas basins. It is seen that the substation's vulnerability depends on the location and basin.

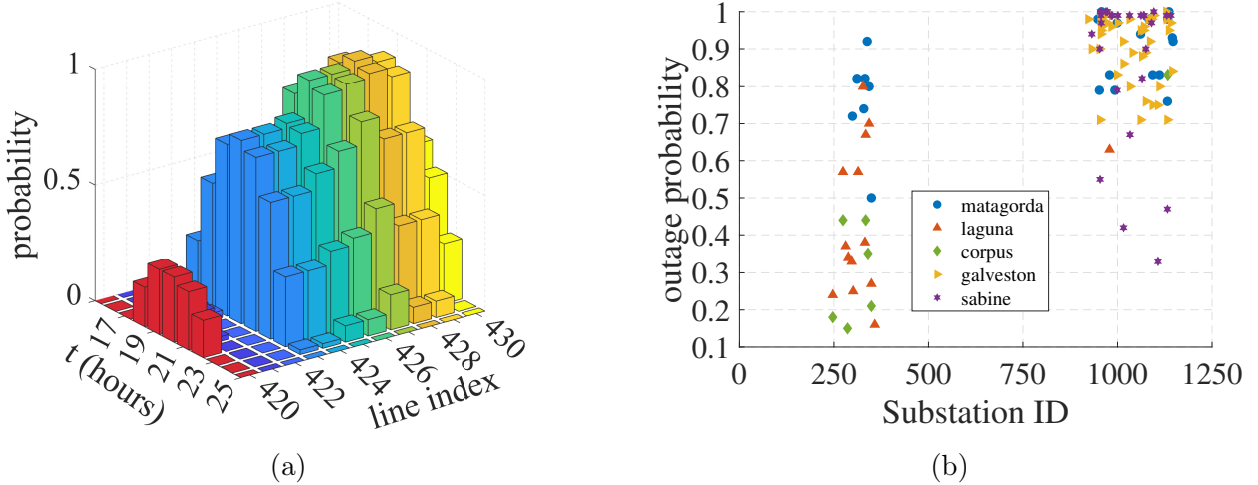


Figure 22: a) Line outage probability for selected lines and the original Harvey's track. b) Substation outage probability for all storm surge scenarios.

It was found that 800 Monte Carlo trials are enough to achieve convergence for any simulation case [61]. Hence, for each ζ , \mathcal{B} , and t , 800 Monte Carlo trials are conducted. Fig. 23 shows the comparison of losses when considering the impact of the hurricane alone with the compound effect of the hurricane and the coastal flood for $\zeta = 1$. It can be observed that considering substation flooding scenarios incur an additional loss of 250 MW by $t = 50$ hours due to substation outages.

Fig. 24 represents the spatiotemporal loss for the compound impact of hurricane and storm surge. The dashed curves represent the loss for all basins for each track, whereas the solid blue curve represents $loss_t$ obtained from (17). The loss is not incurred until $t = 12$ for any ζ under consideration, and the increase is significant once the hurricane moves inland, followed by the compounded impact of storm surge. The loss increases from $loss_{12} = 9.4072$ MW to $loss_{22} = 5536.1$ MW before saturating at $loss_{40} = 6761.97$ MW as the intensity of



Figure 23: Overall loss comparison between the impact of hurricane alone and the compound impact of the hurricane and coastal flood for $\zeta = 1$.

the extreme events decreases.



Figure 24: Time-varying loss for each hurricane track. For each track, the loss at each time step also includes the expected value of loss over entire flood basins.

4 Temporal Alternating Direction Method of Multipliers (tADMM)

4.1 Introduction and Motivation

Multi-period optimal power flow (MPOPF) problems are computationally challenging due to the coupling of variables across time periods through energy storage devices, such as batteries. The temporal coupling arises from the state-of-charge (SOC) dynamics, which link the battery's energy level at each time step to its charging/discharging decisions throughout the entire planning horizon. For large-scale distribution networks with multiple time periods, solving the centralized MPOPF problem becomes intractable.

The Alternating Direction Method of Multipliers (ADMM) is a powerful decomposition technique for solving large-scale convex optimization problems [71, 72]. ADMM is particularly effective for problems that can be decomposed into smaller, more manageable subproblems. The temporal ADMM (tADMM) approach adapts the classical ADMM framework to decompose the MPOPF problem across the temporal dimension, enabling parallel computation of individual time-step subproblems while maintaining consensus on the battery SOC trajectories.

The key insight of tADMM is that while spatial network constraints (power flow equations, voltage limits) are local to each time step, the temporal coupling through battery SOC can be handled through consensus variables. Each time-step subproblem maintains its own local copy of the battery SOC trajectory, and these local copies are coordinated through a global consensus variable that is updated iteratively. This decomposition structure allows for:

- **Parallel computation:** Each time-step subproblem can be solved independently and in parallel
- **Scalability:** Computational complexity grows more favorably with the number of time periods compared to centralized approaches
- **Modularity:** The framework can accommodate different network models (LinDist-Flow, copper plate) without changing the decomposition structure

4.2 LinDistFlow MPOPF with tADMM

4.2.1 Problem Overview

The Temporal ADMM (tADMM) algorithm decomposes the multi-period optimal power flow problem for distribution networks into T subproblems, each corresponding to one time period. This formulation uses the linearized DistFlow model to capture network physics including voltage drops and reactive power flows. The algorithm maintains consensus on battery state-of-charge (SOC) trajectories across all subproblems through an iterative update procedure.

4.2.2 Variable Color Coding

To clearly distinguish the different types of variables in the tADMM formulation, we use the following color-coding scheme:

- $\mathbf{B}_j^{t_0}[t]$ (Blue): Local SOC variables for battery j in subproblem t_0 , evaluated at time t . These are the primal variables optimized in each subproblem.
- $\hat{\mathbf{B}}_j[t]$ (Red): Global consensus SOC for battery j at time t . This represents the agreed-upon SOC trajectory that all subproblems aim to converge to.
- $\mathbf{u}_j^{t_0}[t]$ (Green): Local scaled dual variables for battery j in subproblem t_0 , for time t . These accumulate the consensus violation and guide convergence.

4.2.3 Sets and Indices

- \mathcal{N} : Set of all nodes (buses)
- \mathcal{L} : Set of all branches (lines)
- \mathcal{L}_1 : Set of branches connected to substation (node 1)
- \mathcal{B} : Set of nodes with batteries
- \mathcal{D} : Set of nodes with PV (DER)
- $\mathcal{T} = \{1, 2, \dots, T\}$: Set of time periods
- $t_0 \in \mathcal{T}$: Index for a specific time period in tADMM decomposition

- $j \in \mathcal{N}$: Node index
- $(i, j) \in \mathcal{L}$: Branch from node i to node j

4.2.4 tADMM Algorithm Structure

The tADMM algorithm follows the consensus-based ADMM framework [71, 72], where the true global problem involves a single consensus variable that is used (partially or fully) by all individual subproblems. In the context of MPOPF, the consensus variable is the battery SOC trajectory, and each time-step subproblem maintains its own local copy of this trajectory.

The algorithm alternates between three update steps at each iteration k :

4.2.4.1 Step 1: Subproblem Update (Blue Variables) In the first update step, we solve each subproblem $t_0 \in \{1, 2, \dots, T\}$ independently and in parallel. Each subproblem optimizes its local copy of the battery SOC trajectory $\mathbf{B}_j^{\text{to}}[\mathbf{t}]$ along with the network variables for its specific time step. The latest values of the global consensus variable $\hat{\mathbf{B}}_j[\mathbf{t}]$ and dual variables $\mathbf{u}_j^{\text{to}}[\mathbf{t}]$ from the previous iteration are used to guide the optimization toward consensus.

For each subproblem $t_0 \in \{1, 2, \dots, T\}$:

$$\begin{aligned} & \min_{\substack{P_{\text{Subs}}^{t_0}, Q_{\text{Subs}}^{t_0}, \\ P_{ij}^{t_0}, Q_{ij}^{t_0}, v_j^{t_0}, q_{D,j}^{t_0, \\ P_{B,j}^t, \mathbf{B}_j^{\text{to}}[\mathbf{t}], \\ \forall j \in \mathcal{B}, t \in \mathcal{T}}} c^{t_0} \cdot P_{\text{Subs}}^{t_0} \cdot P_{\text{BASE}} \cdot \Delta t + C_B \sum_{j \in \mathcal{B}} (P_{B,j}^{t_0})^2 \cdot P_{\text{BASE}}^2 \cdot \Delta t \\ & + \frac{\rho}{2} \sum_{j \in \mathcal{B}} \sum_{t=1}^T \left(\mathbf{B}_j^{\text{to}}[\mathbf{t}] - \hat{\mathbf{B}}_j[\mathbf{t}] + \mathbf{u}_j^{\text{to}}[\mathbf{t}] \right)^2 \end{aligned} \quad (18)$$

Subject to:

Spatial Network Constraints (only for time t_0):

$$\text{Real power balance (substation): } P_{\text{Subs}}^{t_0} - \sum_{(1,j) \in \mathcal{L}_1} P_{1j}^{t_0} = 0 \quad (19)$$

$$\begin{aligned} \text{Real power balance (nodes): } P_{ij}^{t_0} - \sum_{(j,k) \in \mathcal{L}} P_{jk}^{t_0} &= P_{B,j}^{t_0} + p_{D,j}^{t_0} - p_{L,j}^{t_0}, \\ &\forall (i, j) \in \mathcal{L}, \end{aligned} \quad (20)$$

$$\text{Reactive power balance (substation): } Q_{\text{Subs}}^{t_0} - \sum_{(1,j) \in \mathcal{L}_1} Q_{1j}^{t_0} = 0 \quad (21)$$

$$\begin{aligned} \text{Reactive power balance (nodes): } Q_{ij}^{t_0} - \sum_{(j,k) \in \mathcal{L}} Q_{jk}^{t_0} &= q_{D,j}^{t_0} - q_{L,j}^{t_0}, \\ &\forall (i, j) \in \mathcal{L}, \end{aligned} \quad (22)$$

$$\text{KVL constraints: } v_i^{t_0} - v_j^{t_0} = 2(r_{ij}P_{ij}^{t_0} + x_{ij}Q_{ij}^{t_0}), \quad \forall (i, j) \in \mathcal{L} \quad (23)$$

$$\text{Voltage limits: } (V_{\min,j})^2 \leq v_j^{t_0} \leq (V_{\max,j})^2, \quad \forall j \in \mathcal{N} \quad (24)$$

$$\begin{aligned} \text{PV reactive limits: } -\sqrt{(S_{D,j})^2 - (p_{D,j}^{t_0})^2} &\leq q_{D,j}^{t_0} \leq \sqrt{(S_{D,j})^2 - (p_{D,j}^{t_0})^2}, \\ &\forall j \in \mathcal{D} \end{aligned} \quad (25)$$

Temporal Battery Constraints (entire horizon $t \in \{1, \dots, T\}$):

$$\text{Initial SOC: } \mathbf{B}_j^{\text{to}}[\mathbf{1}] = B_{0,j} - P_{B,j}^1 \cdot \Delta t, \quad \forall j \in \mathcal{B} \quad (26)$$

$$\text{SOC trajectory: } \mathbf{B}_j^{\text{to}}[\mathbf{t}] = \mathbf{B}_j^{\text{to}}[\mathbf{t-1}] - P_{B,j}^t \cdot \Delta t, \quad \forall t \in \{2, \dots, T\}, j \in \mathcal{B} \quad (27)$$

$$\begin{aligned} \text{SOC limits: } \text{SOC}_{\min,j} \cdot B_{\text{rated},j} &\leq \mathbf{B}_j^{\text{to}}[\mathbf{t}] \leq \text{SOC}_{\max,j} \cdot B_{\text{rated},j}, \\ &\forall t \in \mathcal{T}, j \in \mathcal{B} \end{aligned} \quad (28)$$

$$\text{Power limits: } -P_{B,\text{rated},j} \leq P_{B,j}^t \leq P_{B,\text{rated},j}, \quad \forall t \in \mathcal{T}, j \in \mathcal{B} \quad (29)$$

Key Formulation Notes:

- **Network variables** ($P_{\text{Subs}}^{t_0}, Q_{\text{Subs}}^{t_0}, P_{ij}^{t_0}, Q_{ij}^{t_0}, v_j^{t_0}, q_{D,j}^{t_0}$) are optimized *only* for time step t_0 , representing the spatial network state at that particular time
- **Battery power** $P_{B,j}^t$ is optimized for the *entire* horizon $t \in \{1, \dots, T\}$ to allow proper accounting of temporal coupling
- **Local SOC trajectory** $\mathbf{B}_j^{\text{to}}[\mathbf{t}]$ is computed for *all* time steps $t \in \{1, \dots, T\}$ based on the battery power decisions

- The ADMM consensus penalty compares the full local trajectory $\mathbf{B}_j^{\text{to}}[\mathbf{t}]$ with the global master copy $\hat{\mathbf{B}}_j[\mathbf{t}]$, penalized by the dual variables $\mathbf{u}_j^{\text{to}}[\mathbf{t}]$
- Each battery $j \in \mathcal{B}$ has its own set of local/global SOC variables and dual variables

4.2.4.2 Step 2: Consensus Update (Red Variables) After all subproblems have been solved in parallel to obtain the latest values of $\mathbf{B}_j^{\text{to}}[\mathbf{t}]$, the global consensus variable $\hat{\mathbf{B}}_j[\mathbf{t}]$ is updated by averaging the local SOC trajectories across all subproblems, adjusted by the dual variables. This update brings the consensus closer to the average of what each subproblem believes the SOC should be.

For each battery $j \in \mathcal{B}$ and each time period $t \in \mathcal{T}$:

$$\hat{\mathbf{B}}_j[\mathbf{t}] = \text{clamp} \left(\frac{1}{T} \sum_{t_0=1}^T (\mathbf{B}_j^{\text{to}}[\mathbf{t}] + \mathbf{u}_j^{\text{to}}[\mathbf{t}]), \underline{B}_j, \bar{B}_j \right) \quad (30)$$

where $\underline{B}_j = \text{SOC}_{\min,j} \cdot B_{\text{rated},j}$ and $\bar{B}_j = \text{SOC}_{\max,j} \cdot B_{\text{rated},j}$. The clamping operation ensures that the consensus variable respects the physical SOC bounds.

4.2.4.3 Step 3: Dual Update (Green Variables) Finally, the dual variables $\mathbf{u}_j^{\text{to}}[\mathbf{t}]$ are updated to accumulate the consensus violation (the difference between local and global SOC). These dual variables act as Lagrange multipliers that enforce consensus in the limit as the algorithm converges.

For each battery $j \in \mathcal{B}$, each subproblem $t_0 \in \mathcal{T}$, and each time period $t \in \mathcal{T}$:

$$\mathbf{u}_j^{\text{to}}[\mathbf{t}] := \mathbf{u}_j^{\text{to}}[\mathbf{t}] + (\mathbf{B}_j^{\text{to}}[\mathbf{t}] - \hat{\mathbf{B}}_j[\mathbf{t}]) \quad (31)$$

These three steps are repeated iteratively: solve subproblems for **blue variables**, update consensus **red variables**, and update dual **green variables**, until convergence is achieved.

4.2.5 Convergence Criteria

Primal Residual (Consensus Violation):

The primal residual measures how well the local SOC trajectories $\mathbf{B}_j^{\text{to}}[\mathbf{t}]$ agree with the global consensus $\hat{\mathbf{B}}_j[\mathbf{t}]$ across all batteries and time steps.

$$\|r^k\|_2 = \frac{1}{|\mathcal{B}|} \sqrt{\sum_{j \in \mathcal{B}} \sum_{t=1}^T \left(\frac{1}{T} \sum_{t_0=1}^T \mathbf{B}_j^{t_0}[\mathbf{t}] - \hat{\mathbf{B}}_j[\mathbf{t}] \right)^2} \leq \epsilon_{\text{pri}} \quad (32)$$

Dual Residual (Consensus Change):

The dual residual measures the change in the consensus variable between iterations, indicating convergence stability.

$$\|s^k\|_2 = \frac{\rho}{|\mathcal{B}|} \sqrt{\sum_{j \in \mathcal{B}} \sum_{t=1}^T \left(\hat{\mathbf{B}}_j^k[\mathbf{t}] - \hat{\mathbf{B}}_j^{k-1}[\mathbf{t}] \right)^2} \leq \epsilon_{\text{dual}} \quad (33)$$

4.3 Copper Plate MPOPF with tADMM (Simplified Case)

4.3.1 Problem Overview

To illustrate the tADMM framework more clearly, we first present a simplified copper plate model where network constraints are neglected, and only a single aggregate power balance is enforced at each time step. The Temporal ADMM (tADMM) algorithm decomposes the multi-period optimal power flow problem into T single-step subproblems, each corresponding to one time period. The hope is to enable parallel computation and improved scalability while still retaining solution optimality. Fig. 25 shows the input data for a 24-hour horizon, including the time-varying electricity cost and load demand profiles used in the copper plate MPOPF formulation.

4.3.2 Variable Color Coding

- \mathbf{B}^{t_0} (Blue): Local SOC variables for subproblem t_0
- $\hat{\mathbf{B}}$ (Red): Global consensus SOC trajectory
- \mathbf{u}^{t_0} (Green): Local scaled dual variables for subproblem t_0

4.3.3 tADMM Algorithm Structure

The algorithm alternates between three update steps following the consensus ADMM framework [71, 72]:

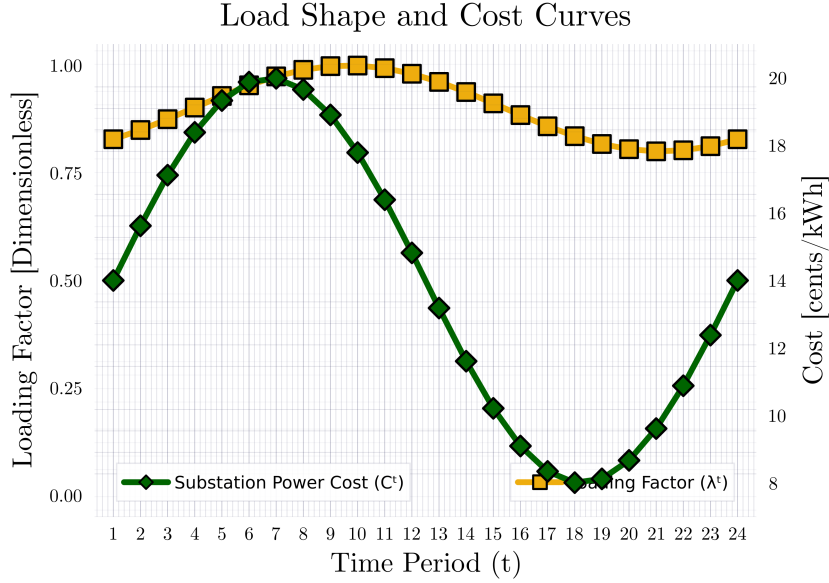


Figure 25: Input curves showing electricity cost and load demand over a 24-hour period.

4.3.3.1 Step 1: Primal Update (Blue Variables) - tADMM Optimization Model

In Update 1 (at iteration k), the latest values of subproblem copies are solved for in parallel using the last known copies of the consensus variable and dual variables – namely $\hat{\mathbf{B}}^{k-1}$ and $\mathbf{u}^{t_0, k-1}$, respectively.

For each subproblem $t_0 \in \{1, 2, \dots, T\}$:

$$\min_{P_{\text{subs}}^{t_0}, P_B^{t_0}, \mathbf{B}^{t_0}} C^{t_0} \cdot P_{\text{subs}}^{t_0} + C_B \cdot (P_B^{t_0})^2 + \frac{\rho}{2} \left\| \mathbf{B}^{t_0} - \hat{\mathbf{B}} + \mathbf{u}^{t_0} \right\|_2^2 \quad (34)$$

Subject to SOC Dynamics for Entire Trajectory:

$$\mathbf{B}^{t_0}[1] = B_0 - P_B^{t_0} \cdot \Delta t \quad (35)$$

$$\mathbf{B}^{t_0}[t] = \mathbf{B}^{t_0}[t-1] - P_B^{t_0} \cdot \Delta t, \quad \forall t \in \{2, \dots, T\} \quad (36)$$

$$P_{\text{subs}}^{t_0} + P_B^{t_0} = P_L[t_0] \quad (37)$$

$$-P_{B,R} \leq P_B^{t_0} \leq P_{B,R} \quad (38)$$

$$\underline{B} \leq \mathbf{B}^{t_0}[t] \leq \bar{B}, \quad \forall t \in \{1, \dots, T\} \quad (39)$$

Key Formulation Notes:

- Each subproblem t_0 optimizes the battery power $P_B^{t_0}$ for *only* time step t_0
- However, the SOC trajectory $\mathbf{B}^{\text{to}}[\mathbf{t}]$ is computed for *all* time steps $t \in \{1, \dots, T\}$
- This ensures that the ADMM penalty term can compare the full trajectory \mathbf{B}^{to} with the consensus $\hat{\mathbf{B}}$
- The power balance constraint is enforced only for the specific time t_0

4.3.3.2 Step 2: Consensus Update (Red Variables) In Update 2 (at iteration k), the latest value of the global consensus variable is computed using the last known copies of the local subproblem SOC trajectories and dual variables – namely $\mathbf{B}_i^{\text{to},k}$ and $\mathbf{u}_i^{\text{to},k-1}$, respectively.

$$\hat{\mathbf{B}}[\mathbf{t}] = \text{clamp} \left(\frac{1}{T} \sum_{t_0=1}^T (\mathbf{B}^{\text{to}}[\mathbf{t}] + \mathbf{u}^{\text{to}}[\mathbf{t}]), \underline{B}, \bar{B} \right) \quad (40)$$

$$\forall t \in \{1, 2, \dots, T-1\} \quad (41)$$

$$\hat{\mathbf{B}}[\mathbf{T}] = B_{T,\text{target}} \quad (\text{if terminal constraint exists}) \quad (42)$$

4.3.3.3 Step 3: Dual Update (Green Variables) In Update 3 (at iteration k), the latest values of local dual variables are computed using the last known copies of the local SOC, global consensus, and previous dual variables – namely $\mathbf{B}_i^{\text{to},k}$, $\hat{\mathbf{B}}^k$, and $\mathbf{u}_i^{\text{to},k-1}$, respectively.

$$\mathbf{u}^{\text{to}}[\mathbf{t}] := \mathbf{u}^{\text{to}}[\mathbf{t}] + (\mathbf{B}^{\text{to}}[\mathbf{t}] - \hat{\mathbf{B}}[\mathbf{t}]) \quad (43)$$

$$\forall t_0 \in \{1, \dots, T\}, \forall t \in \{1, \dots, T\} \quad (44)$$

After every subproblem is solved once to get the latest values of $\mathbf{B}_1, \mathbf{B}_2, \dots, \mathbf{B}_B$, the value of the consensus variable $\hat{\mathbf{B}}$ is updated. Next, the dual variables $\mathbf{u}_1, \mathbf{u}_2, \dots, \mathbf{u}_B$ are updated. This process repeats until convergence.

4.4 Numerical Results

4.4.1 Battery Actions and Convergence Analysis

To validate the tADMM approach, we present numerical results for the copper plate MPOPF problem with a 24-hour planning horizon. The test case includes a single battery energy storage system with time-varying electricity prices and load demands as shown in Fig. 25.

Fig. 26 shows the optimal battery charging and discharging actions obtained from solving the centralized (brute force) MPOPF problem. The battery strategically charges during low-cost periods (typically during nighttime and early morning hours) and discharges during high-cost periods (peak demand hours in the afternoon and evening) to minimize the overall energy cost over the 24-hour horizon. This behavior demonstrates the value of energy arbitrage enabled by battery storage.

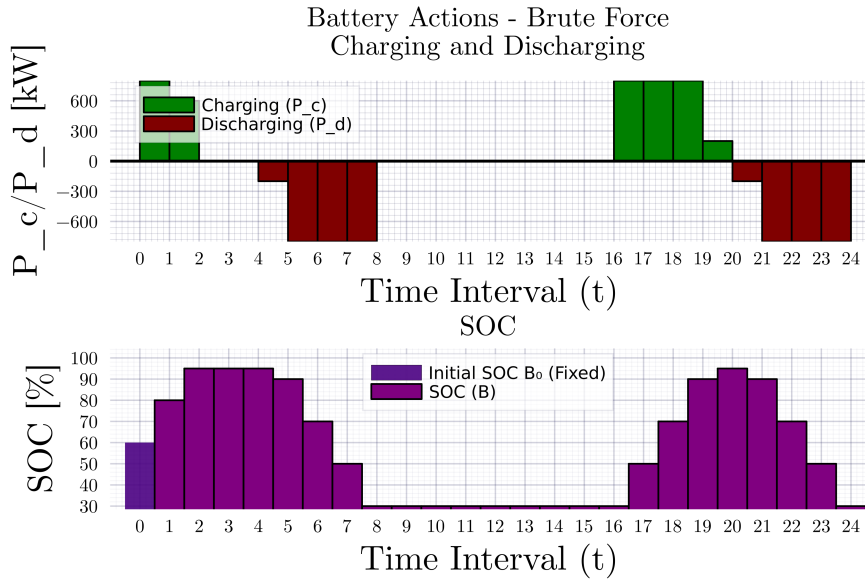


Figure 26: Optimal battery power actions (brute force centralized solution) for copper plate MPOPF over 24-hour horizon. Positive values indicate discharging (supplying power), while negative values indicate charging (consuming power).

Fig. 27 presents the battery actions obtained using the tADMM algorithm, demonstrating that the decomposition approach converges to a solution that closely matches the centralized optimal solution. The close agreement between the two solutions validates the effectiveness of the tADMM decomposition for this problem class. Minor differences, if any, are within the specified convergence tolerances.

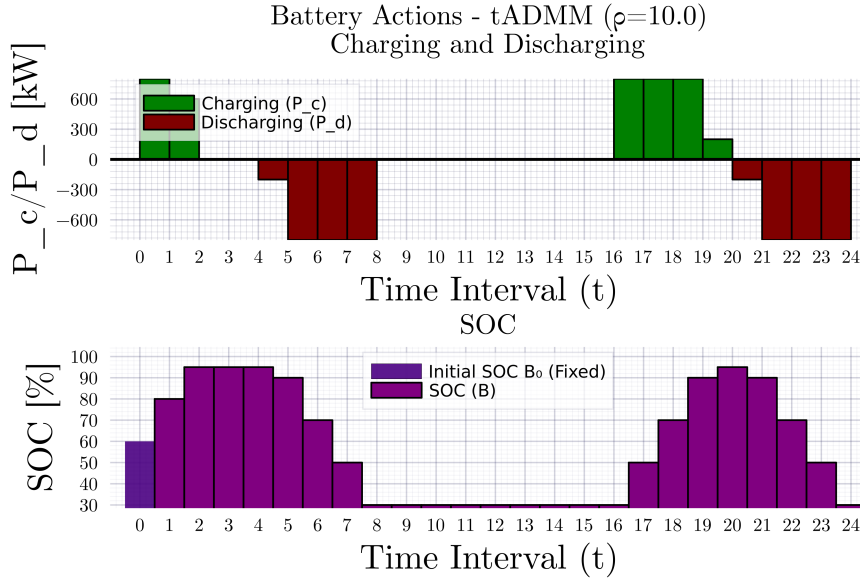


Figure 27: Battery power actions obtained using tADMM for copper plate MPOPF over 24-hour horizon. The solution converges to match the centralized optimal solution.

Fig. 28 illustrates the convergence behavior of the tADMM algorithm, showing how the primal and dual residuals decrease over iterations until they satisfy the specified convergence tolerances ($\epsilon_{\text{pri}} = 10^{-3}$ and $\epsilon_{\text{dual}} = 10^{-3}$). The algorithm typically converges within a few dozen iterations, demonstrating good computational efficiency. The primal residual (consensus violation) decreases as the local SOC trajectories \mathbf{B}^{t_0} converge to the global consensus $\hat{\mathbf{B}}$, while the dual residual tracks the stability of the consensus variable across iterations.

4.5 Convergence Criteria

The algorithm terminates when both residuals fall below specified thresholds:

4.5.1 Convergence Criteria

The algorithm terminates when both residuals fall below specified thresholds:

Primal Residual (Consensus Violation):

The primal residual measures how well the local SOC trajectories \mathbf{B}^{t_0} agree with the global consensus $\hat{\mathbf{B}}$. A small primal residual indicates that all subproblems have converged to a consistent SOC trajectory.

$$\|r^k\|_2 = \left\| \text{vec} \left(\left\{ \mathbf{B}^{t_0} - \hat{\mathbf{B}} \right\}_{t_0=1}^T \right) \right\|_2 \leq \epsilon_{\text{pri}} \quad (45)$$

Dual Residual (Consensus Change):

The dual residual measures how much the consensus variable $\hat{\mathbf{B}}$ is changing between iterations. A small dual residual indicates that the consensus has stabilized.

$$\|s^k\|_2 = \rho \left\| \hat{\mathbf{B}}^k - \hat{\mathbf{B}}^{k-1} \right\|_2 \leq \epsilon_{\text{dual}} \quad (46)$$

4.6 Algorithm Parameters

4.6.1 Objective Function Components

The tADMM objective function for each subproblem t_0 consists of three terms:

$$\text{Energy Cost: } C^{t_0} \cdot P_{\text{subs}}^{t_0} \cdot \Delta t \quad (47)$$

$$\text{Battery Quadratic Cost: } C_B \cdot (P_B^{t_0})^2 \cdot \Delta t \quad (48)$$

$$\text{ADMM Penalty: } \frac{\rho}{2} \left\| B^{t_0} - \hat{B} + u^{t_0} \right\|_2^2 \quad (49)$$

Where:

- C^{t_0} : Energy price at time t_0 [\$/kWh]
- C_B : Battery quadratic cost coefficient [\$/kW²/h] (typically $10^{-6} \times \min(C^t)$)
- ρ : ADMM penalty parameter

The battery quadratic cost term $C_B \cdot (P_B^{t_0})^2$ serves as a regularization to:

1. Prevent excessive battery cycling
2. Encourage smoother power trajectories
3. Improve numerical conditioning of the optimization problem

4.6.2 Algorithmic Parameters

- **Penalty Parameter:** ρ (typically 0.1 to 10.0)
- **Primal Tolerance:** $\epsilon_{\text{pri}} = 10^{-3}$
- **Dual Tolerance:** $\epsilon_{\text{dual}} = 10^{-3}$
- **Maximum Iterations:** 1000

4.7 Appendix: Full Variable and Parameter Definitions

4.7.1 System Bases

$$\text{kV}_B = \frac{4.16}{\sqrt{3}} \text{ kV (phase-to-neutral)} \quad (50)$$

$$\text{kVA}_B = 1000 \text{ kVA} \quad (51)$$

$$P_{\text{BASE}} = 1000 \text{ kW} \quad (52)$$

$$E_{\text{BASE}} = 1000 \text{ kWh per hour} \quad (53)$$

4.7.2 SOC Bound Definitions

$$\underline{B} = \text{SOC}_{\min} \cdot E_{\text{Rated}} \quad (54)$$

$$\overline{B} = \text{SOC}_{\max} \cdot E_{\text{Rated}} \quad (55)$$

4.7.3 Physical Interpretation

- $P_B[t] > 0$: Battery discharging (providing power to the system)
- $P_B[t] < 0$: Battery charging (consuming power from the system)
- $B[t]$: Battery state of charge at the end of period t
- $\underline{B} = \text{SOC}_{\min} \cdot E_{\text{Rated}}$: Lower SOC bound
- $\overline{B} = \text{SOC}_{\max} \cdot E_{\text{Rated}}$: Upper SOC bound

4.8 Summary and Discussion

The temporal ADMM (tADMM) approach provides an effective decomposition framework for solving multi-period optimal power flow problems with energy storage. The key advantages of this approach include:

- **Parallelization:** Each time-step subproblem can be solved independently and in parallel, enabling computational speedup on multi-core processors or distributed computing platforms
- **Modularity:** The decomposition structure is flexible and can accommodate different network models (LinDistFlow, AC power flow, copper plate) without changing the temporal decomposition framework
- **Scalability:** The computational complexity scales more favorably with the number of time periods compared to solving the full centralized problem
- **Convergence guarantees:** For convex formulations, ADMM provides theoretical convergence guarantees to the global optimum [71, 72]

The numerical results demonstrate that tADMM successfully decomposes the temporal coupling through battery SOC while maintaining solution optimality. The algorithm converges within a reasonable number of iterations, and the final solution matches the centralized optimal solution within the specified tolerances. This validates the effectiveness of the consensus-based decomposition for handling temporal coupling in MPOPF problems.

4.8.1 Implementation Status

The tADMM framework has been developed and tested with varying levels of network model complexity:

- **Copper Plate Model (Completed):** The tADMM algorithm has been successfully implemented and tested for the simplified copper plate MPOPF problem. The numerical results presented in Figs. 26, 27, and 28 demonstrate successful convergence to the optimal solution, validating the temporal decomposition approach.
- **LinDistFlow Model (In Progress):** The tADMM formulation with the linearized DistFlow model [73] is currently being implemented. This will incorporate spatial

network constraints including voltage limits, line flow limits, and reactive power constraints while maintaining the temporal decomposition structure.

- **Nonlinear Branch Flow Model (Planned):** Future work will extend the tADMM framework to the SOCP-relaxed nonlinear branch flow model (BFM) [4]. This represents the true nonlinear MPOPF problem with exact AC power flow physics. The BFM formulation will provide a more accurate representation of distribution network behavior while benefiting from the computational advantages of temporal decomposition. This will showcase the full potential of tADMM for solving realistic large-scale MPOPF problems with complex network constraints.

Future extensions of this work will focus on:

- Completing the LinDistFlow implementation and validating performance on realistic distribution networks
- Implementing the SOCP-relaxed BFM formulation with tADMM decomposition
- Applying tADMM to larger distribution networks with multiple batteries and renewable energy sources
- Investigating adaptive penalty parameter selection strategies to improve convergence speed
- Integrating spatial decomposition techniques with temporal decomposition for enhanced scalability

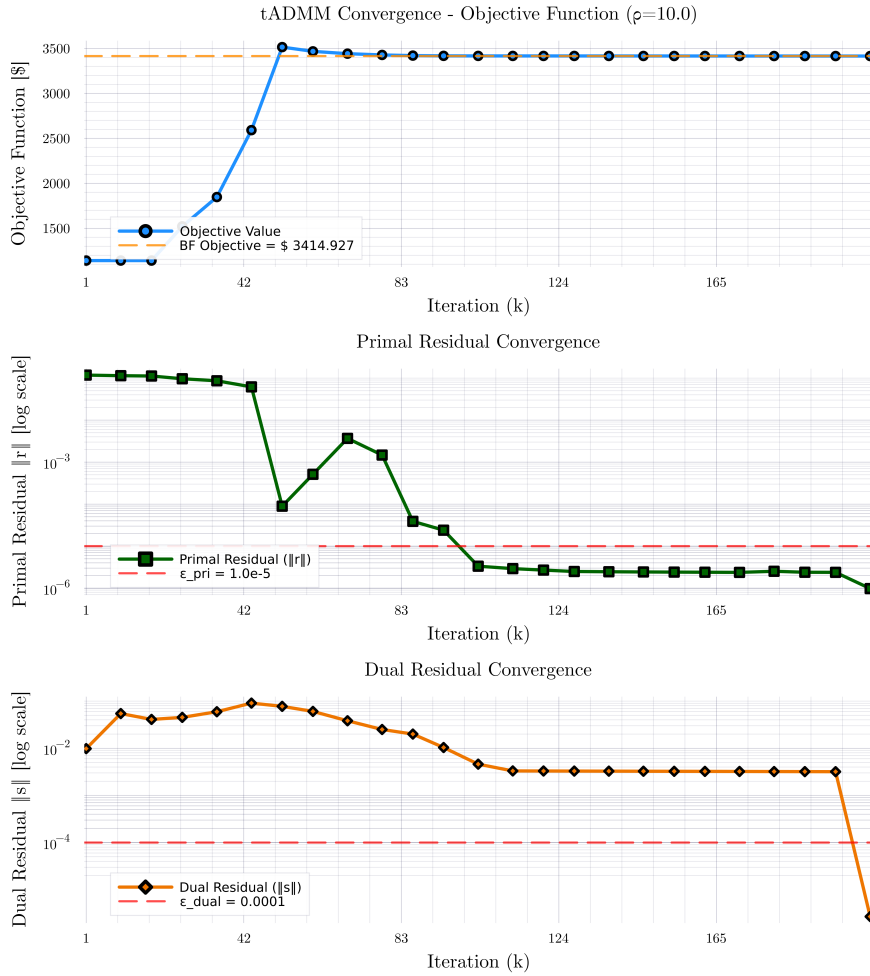


Figure 28: Convergence curves showing primal and dual residuals for tADMM algorithm. Both residuals decrease monotonically and satisfy the convergence criteria.

5 Future Works

The proposed future work aims to extend the temporal decomposition framework developed in this research to larger and more complex power distribution systems. The timeline for completion spans three semesters from Fall 2025 through Summer 2026, culminating in dissertation preparation and defense. The work is organized into three main tasks that progressively scale the methodology and conclude the doctoral research.

5.1 Task 1: Temporal Decomposition for Medium Sized Balanced Three-Phase Systems

The first task focuses on developing and validating the temporal decomposition approach for medium-scale distribution systems assuming balanced three-phase conditions. So far the mathematical framework for temporal decomposition using tADMM has been established, extending the concepts developed in earlier work to handle time-coupled constraints and multi-period optimization problems. The formulation phase will establish the theoretical foundations and decomposition strategy.

Following the formulation, implementation and testing will be conducted on the IEEE 123-bus single-phase test system. This medium-scale system provides sufficient complexity to validate the decomposition approach while remaining computationally tractable for initial testing. The implementation will focus on developing efficient algorithms and testing convergence properties. This task is scheduled for completion during Fall 2025.

5.2 Task 2: Temporal Decomposition for Large Sized Unbalanced Three-Phase Systems

The second task scales the temporal decomposition methodology to large-scale three-phase distribution systems. Building on the insights from Task 1, this phase will formulate the decomposition approach specifically for three-phase unbalanced systems, accounting for the additional complexity of phase coupling and imbalance.

The implementation and testing will be performed on the IEEE 9500-bus three-phase test system, which represents a realistic large-scale distribution network. This task will demonstrate the scalability of the temporal decomposition approach and validate its effectiveness on industry-relevant system sizes. The work is planned for completion during Spring 2026.

5.3 Task 3: Concluding Research and Dissertation

The final task encompasses completion of remaining research activities and dissertation preparation. This includes finishing the investigation of differential dynamic programming (DDP) methods, conducting a comprehensive literature review on novel temporal decomposition methods in power systems, and completing any remaining implementations or case studies.

The dissertation preparation and defense phase will synthesize all research contributions, document the methodologies and results, and prepare for the final defense. This task spans from late Spring 2026 through Summer 2026, concluding the doctoral research program.

5.4 Timeline

The timeline for the research efforts as detailed in Section 5 is shown in Fig. 29.

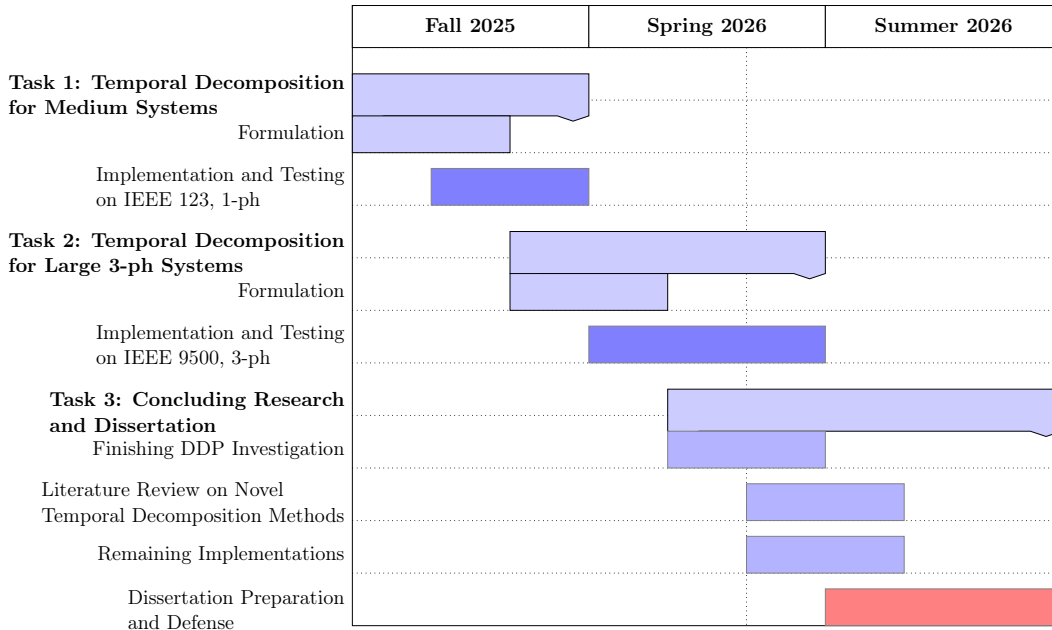


Figure 29: Gantt chart showing execution plan for future works.

6 Biography

Aryan Ritwajeet Jha received the B.E. degree in Electrical and Electronics Engineering from the Birla Institute of Technology and Science (BITS) Pilani, India, in 2020. He is currently pursuing his Ph.D. in Electrical Engineering at Washington State University, Pullman, WA, USA. His research interests include power distribution system optimization, scalable decomposition algorithms for large-scale non-linear optimization and optimization solvers.

6.1 Publications

1. **Jha, A. R.**, Paul, S., & Dubey, A. . Spatially Distributed Multi-Period Optimal Power Flow with Battery Energy Storage Systems. 2024 56th North American Power Symposium (NAPS). IEEE. doi: 10.1109/NAPS61145.2024.10741846 [1]
2. **Jha, A. R.**, Paul, S., & Dubey, A. . Analyzing the Performance of Linear and Nonlinear Multi -Period Optimal Power Flow Models for Active Distribution Networks. 2025 IEEE North-East India International Energy Conversion Conference and Exhibition (NE-IECCE). IEEE. doi: 10.1109/NE-IECCE64154.2025.11183479 [8]

6.2 Program of Study Course Work

Course Number and Name	Semester	Instructor	Grade
E_E 507 Random Processes in Engineering	Fall 2022	Prof. Sandip Roy	A
E_E 521 Analysis of Power Systems	Fall 2022	Prof. Noel Schulz	A
E_E 523 Power Systems Stability	Spring 2023	Prof. Mani V. Venkatasubramanian	A
MATH 564 Convex and Nonlinear Optimization	Fall 2023	Prof. Tom Asaki	A
MATH 565 Nonsmooth Analysis and Optimization	Spring 2024	Prof. Tom Asaki	A-
CPT_S 530 Numerical Analysis ¹	Fall 2025	Prof. Alexander Panchenko	
E_E 582 Electrical Systems Modelling and Simulation ¹	Fall 2025	Prof. Seyedmilad Ebrahimi	
E_E 595 Directed Studies in Electrical Engineering ¹	Fall 2025	Prof. Rahul K. Gupta	

¹

¹currently taking this semester

Appendix

In Section .1 from Equations (56) to (68), the full optimization formulation for the Multi-Period Optimal Power Flow (MPOPF) problem using the LinDistFlow model is presented.

.1 Full MPOPF Formulation with LinDistFlow

Sets:

- \mathbb{N} : Set of all buses, with substation bus $j_1 \in \mathbb{N}$
- $\mathbb{N} \setminus \{j_1\}$: Set of non-substation buses
- \mathbb{L} : Set of all branches (directed edges)
- \mathbb{L}_1 : Set of branches directly connected to substation bus j_1
- $\mathbb{L} \setminus \mathbb{L}_1$: Set of branches not connected to substation
- \mathbb{B} : Set of buses with battery storage
- \mathbb{D} : Set of buses with distributed energy resources (DERs)
- \mathbb{T} : Set of time periods $\{1, 2, \dots, T\}$

Objective Function:

$$\min \sum_{t \in \mathbb{T}} C^t P_{\text{Subs}}^t \Delta t + \sum_{t \in \mathbb{T}} \sum_{j \in \mathbb{B}} C_B (P_{B_j}^t)^2 \Delta t \quad (56)$$

Subject to:

Power Balance at Substation Bus ($j = j_1$):

$$P_{\text{Subs}}^t - \sum_{(j_1, k) \in \mathbb{L}_1} P_{j_1 k}^t = 0, \quad \forall t \in \mathbb{T} \quad (57)$$

$$Q_{\text{Subs}}^t - \sum_{(j_1, k) \in \mathbb{L}_1} Q_{j_1 k}^t = 0, \quad \forall t \in \mathbb{T} \quad (58)$$

Power Balance at Non-Substation Buses ($j \in \mathbb{N} \setminus \{j_1\}$):

$$\sum_{(j, k) \in \mathbb{L}} P_{jk}^t - \sum_{(i, j) \in \mathbb{L}} P_{ij}^t = P_{B_j}^t + p_{D_j}^t - p_{L_j}^t, \quad \forall j \in \mathbb{N}, \forall t \in \mathbb{T} \quad (59)$$

$$\sum_{(j, k) \in \mathbb{L}} Q_{jk}^t - \sum_{(i, j) \in \mathbb{L}} Q_{ij}^t = q_{D_j}^t - q_{L_j}^t, \quad \forall j \in \mathbb{N}, \forall t \in \mathbb{T} \quad (60)$$

Voltage Drop (LinDistFlow KVL):

$$v_j^t = v_i^t - 2(r_{ij}P_{ij}^t + x_{ij}Q_{ij}^t), \quad \forall(i, j) \in \mathbb{L}, \forall t \in \mathbb{T} \quad (61)$$

Substation Voltage:

$$v_{j1}^t = v_{\text{nom}}^2, \quad \forall t \in \mathbb{T} \quad (62)$$

Voltage Limits:

$$(v_{\min})^2 \leq v_j^t \leq (v_{\max})^2, \quad \forall j \in \mathbb{N}, \forall t \in \mathbb{T} \quad (63)$$

Battery State of Charge:

$$B_j^t = B_j^{t-1} - P_{B_j}^t \Delta t, \quad \forall j \in \mathbb{B}, \forall t \in \mathbb{T} \setminus \{1\} \quad (64)$$

$$B_j^1 = B_{j,0}, \quad \forall j \in \mathbb{B} \quad (65)$$

Battery Constraints:

$$\text{SOC}_{\min} B_{R_j} \leq B_j^t \leq \text{SOC}_{\max} B_{R_j}, \quad \forall j \in \mathbb{B}, \forall t \in \mathbb{T} \quad (66)$$

$$-P_{B_{R_j}} \leq P_{B_j}^t \leq P_{B_{R_j}}, \quad \forall j \in \mathbb{B}, \forall t \in \mathbb{T} \quad (67)$$

PV Reactive Power Limits:

$$-\sqrt{S_{D_{R_j}}^2 - (p_{D_j}^t)^2} \leq q_{D_j}^t \leq \sqrt{S_{D_{R_j}}^2 - (p_{D_j}^t)^2}, \quad \forall j \in \mathbb{D}, \forall t \in \mathbb{T} \quad (68)$$

Variables:

- $P_{\text{Subs}}^t, Q_{\text{Subs}}^t$: Substation real and reactive power at time t
- P_{ij}^t, Q_{ij}^t : Sending-end real and reactive power flow on branch (i, j) at time t
- v_j^t : Squared voltage magnitude at bus j at time t
- $P_{B_j}^t$: Battery power at bus j at time t (positive = discharging)
- B_j^t : Battery state of charge at bus j at time t
- $q_{D_j}^t$: PV reactive power injection at bus j at time t

Parameters:

- C^t : Energy cost at time t (\$/kWh)
- C_B : Battery degradation cost coefficient
- Δt : Time step duration

- r_{ij}, x_{ij} : Branch resistance and reactance
- $p_{L_j}^t, q_{L_j}^t$: Load real and reactive power at bus j at time t
- $p_{D_j}^t$: PV real power generation at bus j at time t
- $B_{R_j}, P_{B_{R_j}}$: Battery energy and power capacity at bus j
- $S_{D_{R_j}}$: PV apparent power capacity at bus j

References

- [1] A. R. Jha, S. Paul, and A. Dubey, “Analyzing the Performance of Linear and Nonlinear Multi-Period Optimal Power Flow Models for Active Distribution Networks,” in *2025 IEEE North-East India International Energy Conversion Conference and Exhibition (NE-IECCE)*. IEEE, pp. 04–06.
- [2] N. Nazir, P. Racherla, and M. Almassalkhi, “Optimal multi-period dispatch of distributed energy resources in unbalanced distribution feeders,” *arXiv*, Jun. 2019.
- [3] A. Agarwal and L. Pileggi, “Large Scale Multi-Period Optimal Power Flow With Energy Storage Systems Using Differential Dynamic Programming,” *IEEE Trans. Power Syst.*, vol. 37, no. 3, pp. 1750–1759, Sep. 2021.
- [4] M. Farivar and S. H. Low, “Branch Flow Model: Relaxations and Convexification—Part I,” *IEEE Trans. Power Syst.*, vol. 28, no. 3, pp. 2554–2564, Apr. 2013.
- [5] S. Gabash and P. Li, “Active-reactive optimal power flow with battery energy storage in distribution systems,” *IEEE Transactions on Power Systems*, vol. 28, no. 3, pp. 2637–2646, 2013.
- [6] N. Nazir and M. Almassalkhi, “Receding-Horizon Optimization of Unbalanced Distribution Systems with Time-Scale Separation for Discrete and Continuous Control Devices,” *2018 Power Systems Computation Conference (PSCC)*, pp. 1–7, Jun. 2018.
- [7] L. Gan, U. Topcu, and S. H. Low, “Convex Relaxation of Optimal Power Flow Part I: Formulations and Equivalence,” in *IEEE Transactions on Power Systems*, 2015, vol. 30, no. 1, pp. 290–301.
- [8] A. R. Jha, S. Paul, and A. Dubey, “Spatially Distributed Multi-Period Optimal Power Flow with Battery Energy Storage Systems,” in *2024 56th North American Power Symposium (NAPS)*. IEEE, pp. 13–15.
- [9] G. Valverde, E. M. G. de Oliveira, A. M. V. de Lara, J. R. S. Peres, and N. Favilla, “Multiperiod optimum power flow for active distribution networks incorporating distributed generation and energy storage systems,” *IEEE Transactions on Industry Applications*, 2021. [Online]. Available: <https://ieeexplore.ieee.org/document/9502092/>
- [10] A. G. B. et al., “Large scale multi-period optimal power flow with energy storage,” *IEEE Transactions on Power Systems*, 2021. [Online]. Available: <https://ieeexplore.ieee.org/document/9549701/>
- [11] ———, “Large scale multi-period optimal power flow with energy storage,” *IEEE Transactions on Power Systems*, 2021. [Online]. Available: <https://ieeexplore.ieee.org/document/9549701/>
- [12] L. W. et al., “Benders decomposition based multi-period distributed optimal power flow for distribution networks,” *Electric Power Systems Research*, vol. 198, p. 107440, 2021.

- [13] G. Kandaperumal and A. K. Srivastava, “Resilience of the electric distribution systems: concepts, classification, assessment, challenges, and research needs,” *IET Smart Grid*, vol. 3, no. 2, pp. 133–143, 2020.
- [14] B. Cai, M. Xie, Y. Liu, Y. Liu, and Q. Feng, “Availability-based engineering resilience metric and its corresponding evaluation methodology,” *Reliability Engineering & System Safety*, vol. 172, pp. 216–224, 2018.
- [15] M. Panteli, C. Pickering, S. Wilkinson, R. Dawson, and P. Mancarella, “Power system resilience to extreme weather: fragility modeling, probabilistic impact assessment, and adaptation measures,” *IEEE Trans. Power Syst.*, vol. 32, no. 5, pp. 3747–3757, 2017.
- [16] M. Wen, Y. Chen, Y. Yang, R. Kang, and Y. Zhang, “Resilience-based component importance measures,” *International Journal of Robust and Nonlinear Control*, vol. 30, no. 11, pp. 4244–4254, 2020.
- [17] S. Espinoza, A. Poulos, and *et al.*, “Seismic resilience assessment and adaptation of the northern chilean power system,” in *2017 IEEE Power & Energy Society General Meeting*. IEEE, 2017, pp. 1–5.
- [18] S. Poudel and A. Dubey, “Critical load restoration using distributed energy resources for resilient power distribution system,” *IEEE Transactions on Power Systems*, vol. 34, no. 1, pp. 52–63, 2018.
- [19] A. Umunnakwe, H. Huang, K. Oikonomou, and K. Davis, “Quantitative analysis of power systems resilience: Standardization, categorizations, and challenges,” *Renewable and Sustainable Energy Reviews*, vol. 149, p. 111252, 2021.
- [20] P. Bajpai, S. Chanda, and A. K. Srivastava, “A novel metric to quantify and enable resilient distribution system using graph theory and choquet integral,” *IEEE Transactions on Smart Grid*, vol. 9, no. 4, pp. 2918–2929, 2018.
- [21] S. Chanda and A. K. Srivastava, “Defining and enabling resiliency of electric distribution systems with multiple microgrids,” *IEEE Transactions on Smart Grid*, vol. 7, no. 6, pp. 2859–2868, 2016.
- [22] H. Gao, Y. Chen, Y. Xu, and C.-C. Liu, “Resilience-oriented critical load restoration using microgrids in distribution systems,” *IEEE Transactions on Smart Grid*, vol. 7, no. 6, pp. 2837–2848, 2016.
- [23] V. Venkataramanan, A. Hahn, and A. Srivastava, “Cp-sam: Cyber-physical security assessment metric for monitoring microgrid resiliency,” *IEEE Transactions on Smart Grid*, vol. 11, no. 2, pp. 1055–1065, 2020.
- [24] M. Panteli and P. Mancarella, “The grid: Stronger, bigger, smarter?: Presenting a conceptual framework of power system resilience,” *IEEE Power and Energy Magazine*, vol. 13, no. 3, pp. 58–66, 2015.

- [25] S. Poudel, A. Dubey, and A. Bose, “Risk-based probabilistic quantification of power distribution system operational resilience,” *IEEE Systems Journal*, vol. 14, no. 3, pp. 3506–3517, 2019.
- [26] A. Kwasinski, “Quantitative model and metrics of electrical grids’ resilience evaluated at a power distribution level,” *Energies*, vol. 9, no. 2, p. 93, Feb. 2016.
- [27] Choquet, G., “Theory of Capacities,” *Annales de l’Institut Fourier*, pp. 131–195, 1953.
- [28] M. Grabisch and C. Labreuche, “A decade of application of the choquet and sugeno integrals in multi-criteria decision aid,” *Annals of Operations Research*, vol. 175, no. 1, pp. 247–286, 2010.
- [29] A. Arif, S. Ma, Z. Wang, J. Wang, S. M. Ryan, and C. Chen, “Optimizing Service Restoration in Distribution Systems With Uncertain Repair Time and Demand,” *IEEE Transactions on Power Systems*, vol. 33, no. 6, pp. 6828–6838, 2018.
- [30] W. Yuan, J. Wang, F. Qiu, C. Chen, C. Kang, and B. Zeng, “Robust Optimization-Based Resilient Distribution Network Planning Against Natural Disasters,” *IEEE Transactions on Smart Grid*, vol. 7, no. 6, pp. 2817–2826, 2016.
- [31] H. Gao, Y. Chen, S. Mei, S. Huang, and Y. Xu, “Resilience-oriented pre-hurricane resource allocation in distribution systems considering electric buses,” *Proceedings of the IEEE*, vol. 105, no. 7, pp. 1214–1233, 2017.
- [32] Q. Zhang, Z. Wang, S. Ma, and A. Arif, “Stochastic pre-event preparation for enhancing resilience of distribution systems,” *Renewable and Sustainable Energy Reviews*, vol. 152, p. 111636, 2021.
- [33] W. Yuan, J. Wang, F. Qiu, C. Chen, C. Kang, and B. Zeng, “Robust optimization-based resilient distribution network planning against natural disasters,” *IEEE Transactions on Smart Grid*, vol. 7, no. 6, pp. 2817–2826, 2016.
- [34] X. Wang, M. Shahidehpour, C. Jiang, and Z. Li, “Resilience enhancement strategies for power distribution network coupled with urban transportation system,” *IEEE Transactions on Smart Grid*, vol. 10, no. 4, pp. 4068–4079, 2018.
- [35] S. Ma *et al.*, “Resilience enhancement of distribution grids against extreme weather events,” *IEEE Transactions on Power Systems*, vol. 33, no. 5, pp. 4842–4853, 2018.
- [36] ———, “Resilience-oriented design of distribution systems,” *IEEE Transactions on Power Systems*, vol. 34, no. 4, pp. 2880–2891, 2019.
- [37] J. Liu, Y. Yu, and C. Qin, “Unified two-stage reconfiguration method for resilience enhancement of distribution systems,” *IET Generation, Transmission & Distribution*, vol. 13, no. 9, pp. 1734–1745, 2019.
- [38] Q. Shi, F. Li, T. Kuruganti, M. M. Olama, J. Dong, X. Wang, and C. Winstead, “Resilience-oriented dg siting and sizing considering stochastic scenario reduction,” *IEEE Transactions on Power Systems*, vol. 36, no. 4, pp. 3715–3727, 2020.

- [39] Q. Zhang, Z. Wang, S. Ma, and A. Arif, “Stochastic pre-event preparation for enhancing resilience of distribution systems,” *Elsevier BV*, vol. 152, p. 111636, Dec. 2021.
- [40] S. Ma *et al.*, “Resilience Enhancement of Distribution Grids Against Extreme Weather Events,” *IEEE Transactions on Power Systems*, vol. 33, no. 5, pp. 4842–4853, 2018.
- [41] B. Taheri, A. Safdarian, M. Moeini-Aghetaie, and M. Lehtonen, “Distribution system resilience enhancement via mobile emergency generators,” *IEEE Transactions on Power Delivery*, vol. 36, no. 4, pp. 2308–2319, 2021.
- [42] P. W. Glynn and D. L. Iglehart, “Importance sampling for stochastic simulations,” *Management science*, vol. 35, no. 11, pp. 1367–1392, 1989.
- [43] R. Rush, J. M. Mulvey, J. E. Mitchell, and T. R. Willemain, “Stratified filtered sampling in stochastic optimization,” *Journal of Applied Mathematics and Decision Sciences*, vol. 4, no. 1, pp. 17–38, 2000.
- [44] D. Urgun, C. Singh, and V. Vittal, “Importance sampling using multilabel radial basis classification for composite power system reliability evaluation,” *IEEE Systems Journal*, vol. 14, no. 2, pp. 2791–2800, 2020.
- [45] R. Preece and J. V. Milanović, “Efficient estimation of the probability of small-disturbance instability of large uncertain power systems,” *IEEE Transactions on Power Systems*, vol. 31, no. 2, pp. 1063–1072, 2016.
- [46] R. Moreno, M. Panteli, P. Mancarella, H. Rudnick, T. Lagos, A. Navarro, F. Ordonez, and J. C. Araneda, “From Reliability to Resilience: Planning the Grid Against the Extremes,” *IEEE Power and Energy Magazine*, vol. 18, no. 4, pp. 41–53, 2020.
- [47] L. C. Coelho, “Linearization of the product of two variables,” *Canada Research Chair in Integrated Logistics*, 2013.
- [48] A. Poudyal, V. Iyengar, D. Garcia-Camargo, and A. Dubey, “Spatiotemporal impact assessment of hurricanes on electric power systems,” in *2022 IEEE Power Energy Society General Meeting (PESGM)*, 2022, pp. 1–5.
- [49] M. D. Powell, S. H. Houston, and I. Ares, “Real-time damage assessment in hurricanes,” in *Preprints, 21st Conf. on Hurricanes and Tropical Meteorology, Miami, FL, Amer. Meteor. Soc*, 1995, pp. 500–502.
- [50] M. Panteli and P. Mancarella, “Modeling and Evaluating the Resilience of Critical Electrical Power Infrastructure to Extreme Weather Events,” *IEEE Systems Journal*, vol. 11, no. 3, pp. 1733–1742, 2017.
- [51] V. L. Parsons, “Stratified sampling,” *Wiley StatsRef: Statistics Reference Online*, pp. 1–11, Feb. 2017.

- [52] J. Ekblom and J. Blomvall, “Importance sampling in stochastic optimization: An application to intertemporal portfolio choice,” *European Journal of Operational Research*, vol. 285, no. 1, pp. 106–119, 2020.
- [53] H. Heitsch and W. Römisch, “A note on scenario reduction for two-stage stochastic programs,” *Operations Research Letters*, vol. 35, no. 6, pp. 731–738, 2007.
- [54] M. Panteli, D. N. Trakas, P. Mancarella, and N. D. Hatziargyriou, “Boosting the power grid resilience to extreme weather events using defensive islanding,” *IEEE Transactions on Smart Grid*, vol. 7, no. 6, pp. 2913–2922, 2016.
- [55] D. N. Trakas, M. Panteli, N. D. Hatziargyriou, and P. Mancarella, “Spatial risk analysis of power systems resilience during extreme events,” *Risk Analysis*, vol. 39, no. 1, pp. 195–211, Oct. 2018.
- [56] H. T. Nguyen, J. W. Muhs, and M. Parvania, “Assessing impacts of energy storage on resilience of distribution systems against hurricanes,” *Journal of Modern Power Systems and Clean Energy*, vol. 7, no. 4, pp. 731–740, 2019.
- [57] L. Souto, J. Yip, W.-Y. Wu, B. Austgen, E. Kutanoglu, J. Hasenbein, Z.-L. Yang, C. W. King, and S. Santoso, “Power system resilience to floods: Modeling, impact assessment, and mid-term mitigation strategies,” *International Journal of Electrical Power & Energy Systems*, vol. 135, p. 107545, 2022.
- [58] A. Shukla, J. Hasenbein, and E. Kutanoglu, “A scenario-based optimization approach for electric grid substation hardening against storm surge flooding,” in *IIE Annual Conference. Proceedings*. Institute of Industrial and Systems Engineers (IISE), 2021, pp. 1004–1009.
- [59] K. Feng, M. Ouyang, and N. Lin, “Tropical cyclone-blackout-heatwave compound hazard resilience in a changing climate,” *Nature Communications*, vol. 13, no. 1, Jul. 2022.
- [60] P. Javanbakht and S. Mohagheghi, “A risk-averse security-constrained optimal power flow for a power grid subject to hurricanes,” *Electric Power Systems Research*, vol. 116, pp. 408–418, 2014.
- [61] A. Poudyal, A. Dubey, V. Iyengar, and D. Garcia-Camargo, “Spatiotemporal impact assessment of hurricanes on electric power systems,” in *2022 IEEE Power & Energy Society General Meeting (PESGM)*, 2022, pp. 1–5.
- [62] K. R. Knapp, M. C. Kruk, D. H. Levinson, H. J. Diamond, and C. J. Neumann, “The international best track archive for climate stewardship (IBTrACS),” *Bulletin of the American Meteorological Society*, vol. 91, no. 3, pp. 363–376, Mar. 2010.
- [63] B. Glahn, A. Taylor, N. Kurkowski, and W. A. Shaffer, “The role of the slosh model in national weather service storm surge forecasting,” *National Weather Digest*, vol. 33, no. 1, pp. 3–14, 2009.

- [64] “Slosh display package.” [Online]. Available: <https://slosh.nws.noaa.gov/sdp/>
- [65] M. Panteli, C. Pickering, S. Wilkinson, R. Dawson, and P. Mancarella, “Power system resilience to extreme weather: Fragility modeling, probabilistic impact assessment, and adaptation measures,” *IEEE Transactions on Power Systems*, vol. 32, no. 5, pp. 3747–3757, 2017.
- [66] *Hazus Flood Technical Manual HAZUS 5.1*, Federal Emergency Management Agency, Jul 2022. [Online]. Available: https://www.fema.gov/sites/default/files/documents/fema_hazus-flood-model-technical-manual-5-1.pdf
- [67] D. N. Bresch and G. Aznar-Siguán, “CLIMADA v1.4.1: towards a globally consistent adaptation options appraisal tool,” *Geoscientific Model Development*, vol. 14, no. 1, pp. 351–363, Jan. 2021.
- [68] “Definition of the NHC Track Forecast Cone.” [Online]. Available: <https://www.nhc.noaa.gov/pdf/sshws.pdf> [Accessed: November 4, 2022]
- [69] A. B. Birchfield, T. Xu, K. M. Gegner, K. S. Shetye, and T. J. Overbye, “Grid structural characteristics as validation criteria for synthetic networks,” *IEEE Transactions on Power Systems*, vol. 32, no. 4, pp. 3258–3265, 2017.
- [70] R. D. Zimmerman, C. E. Murillo-Sánchez, and R. J. Thomas, “Matpower: Steady-state operations, planning, and analysis tools for power systems research and education,” *IEEE Transactions on Power Systems*, vol. 26, no. 1, pp. 12–19, 2011.
- [71] “ADMM,” Oct. 2025, [Online; accessed 28. Oct. 2025]. [Online]. Available: <https://stanford.edu/~boyd/admm.html>
- [72] “Index of /~ryantibs/convexopt-F16/lectures,” Oct. 2025, [Online; accessed 28. Oct. 2025]. [Online]. Available: <https://www.stat.cmu.edu/~ryantibs/convexopt-F16/lectures>
- [73] M. E. Baran and F. F. Wu, “Optimal capacitor placement on radial distribution systems,” *IEEE Transactions on Power Delivery*, vol. 4, no. 1, pp. 725–734, 1989.